HEALTH AND MEDICINE

ROS-responsive nanogels enable inhaled CD24 immunotherapy for selective hyperinflammation suppression in severe pneumonia

Xin Wang[1]†, Xiaofei Zhao[1]†, Fan Zhang[2]†, Siyu Wang[1], Fenghua Meng[1], Chao Deng[1]*, Mingzhou Ye[2]*, Zhiyuan Zhong[1,3]*

Acute pneumonia triggered by pathogen infection and lung injury persists as a critical global life-threatening issue. Cluster of differentiation 24 (CD24), by selectively inhibiting the inflammatory response associated with damage-associated molecular patterns (DAMPs) through the interaction with Siglec, has appeared as a unique paradigm to alleviate acute pneumonia, yet its effective pulmonary delivery remains challenging. Here, we report on reactive oxygen species (ROS)–responsive and mucus-penetrable nanogels (ROSμNG) for pulmonary CD24 delivery to rescue acute pneumonia by selective inhibition of hyperinflammatory response. CD24-loaded nanogels (CD24-ROSμNG) exhibit excellent stability during nebulization, efficient mucus penetration, and inflammation-triggered CD24 release, affording over 80% drug enrichment in lung tissues through nebulization inhalation. In lipopolysaccharide-induced severe acute pneumonia mouse models, nebulized CD24-ROSμNG effectively attenuates cytokine storm, suppresses DAMP-mediated inflammation, and mitigates lung injury, achieving an over 3.5-fold increase in survival rate compared to intravenous administration of over 12-fold higher dose of free CD24. In an H1N1 virus influenza model, CD24-ROSμNG not only prevents cytokine storm but also preserves neutrophil-mediated viral clearance by limiting excessive neutrophil extracellular trap formation, thereby avoiding uncontrolled inflammation while maintaining antiviral defenses. These inhalable CD24 nanogels establish a strategy to manage pulmonary hyperinflammatory disorders.

INTRODUCTION

Acute pneumonia caused by infections and lung injury persists as a critical global health threat (*1*, *2*). As a leading cause of death worldwide, severe cases involve dysregulated immunity and cytokine storms (*3*, *4*), which not only exacerbate lung damage but also trigger systemic complications such as acute respiratory distress syndrome (ARDS) and sepsis (*5*, *6*). Current treatments primarily use broad-spectrum corticosteroids [e.g., dexamethasone (Dex)] to suppress inflammation, but they pose substantial risks of weakened immunity, metabolic disorders, and osteoporosis complications (*7*, *8*). Emerging targeted therapies [e.g., anakinra (*9*), tocilizumab (*10*), and BDB-001 (*11*)] offer reduced side effects but remain limited by compensatory activation of alternative immune pathways stemming from their single-target nature, ultimately compromising therapeutic efficacy (*12*).

Central to the pathology of acute pneumonia is the dysregulated amplification of the immune response by damage-associated molecular patterns (DAMPs). These endogenous alarm signals drive unchecked cytokine production and propagate tissue injury, culminating in widespread structural damage (*13*, *14*). Among emerging therapeutic strategies, cluster of differentiation 24 (CD24) has distinguished itself as a unique innate immune regulator. By binding DAMPs and concurrently engaging the Siglec-G/Src homology region 2 domain-containing phosphatase-1 (SHP-1) axis to suppress nuclear factor κB (NF-κB) signaling, CD24 tempers sterile inflammation while preserving pathogen-associated molecular pattern (PAMP)–driven antimicrobial immunity (*15*, *16*). In this way, CD24 offers the rare ability to reconcile anti-inflammatory efficacy with maintenance of host defense. Clinical studies have underscored this potential: Recombinant CD24 reduced progression to severe disease and accelerated recovery in COVID-19–related pneumonia (*17*), while inhaled exosome-based CD24 therapy enabled rapid improvement in critically ill patients, with more than 80% discharged from intensive care within 1 week (*18*). Despite such encouraging signals, formidable translational barriers remain. Intravenous administration distributes CD24 systemically, limiting effective concentrations in the lung and raising the risk of off-target effects (*19*). Pulmonary delivery circumvents hepatic first-pass metabolism and enhances alveolar targeting but faces intrinsic protein fragility during aerosolization, thickened mucus barriers in inflamed airways, and unregulated therapeutic release (*20*, *21*). Exosome formulations partially address these issues yet confront heterogeneity, scale-up challenges, and regulatory complexity, underscoring the critical demand for advanced pulmonary delivery systems for therapeutic proteins like CD24 (*22*, *23*).

In this study, we have developed an inhalable, reactive oxygen species (ROS)–responsive and mucus-penetrable nanogel platform (ROSμNG) for lung-targeted CD24 delivery to rescue acute pneumonia by selective suppression of DAMP-driven inflammation (Fig. 1). Constructed via catalyst-free click chemistry between hyaluronic acid dibenzocyclooctyne derivatives (HA-DBCO) and azide/thioketal-functionalized four-arm poly(ethylene glycol) (4arm PEG-TK-N_3), this covalent nanogel matrix protects CD24 against

[1]Biomedical Polymers Laboratory, and Jiangsu Key Laboratory of Advanced Functional Polymer Materials, College of Chemistry, Chemical Engineering, and Materials Science, and State Key Laboratory of Radiation Medicine and Protection, Soochow University, Suzhou 215123, China. [2]Division of Nanobiomedicine, Suzhou Institute of Nano-Tech and Nano-Bionics, Chinese Academy of Sciences, Suzhou 215123, Jiangsu Province, China. [3]College of Pharmaceutical Sciences, Soochow University, Suzhou 215123, China.
*Corresponding author. Email: cdeng@suda.edu.cn (C.D.); mzye2021@sinano.ac.cn (M.Y.); zyzhong@suda.edu.cn (Z.Z.)
†These authors contributed equally to this work.

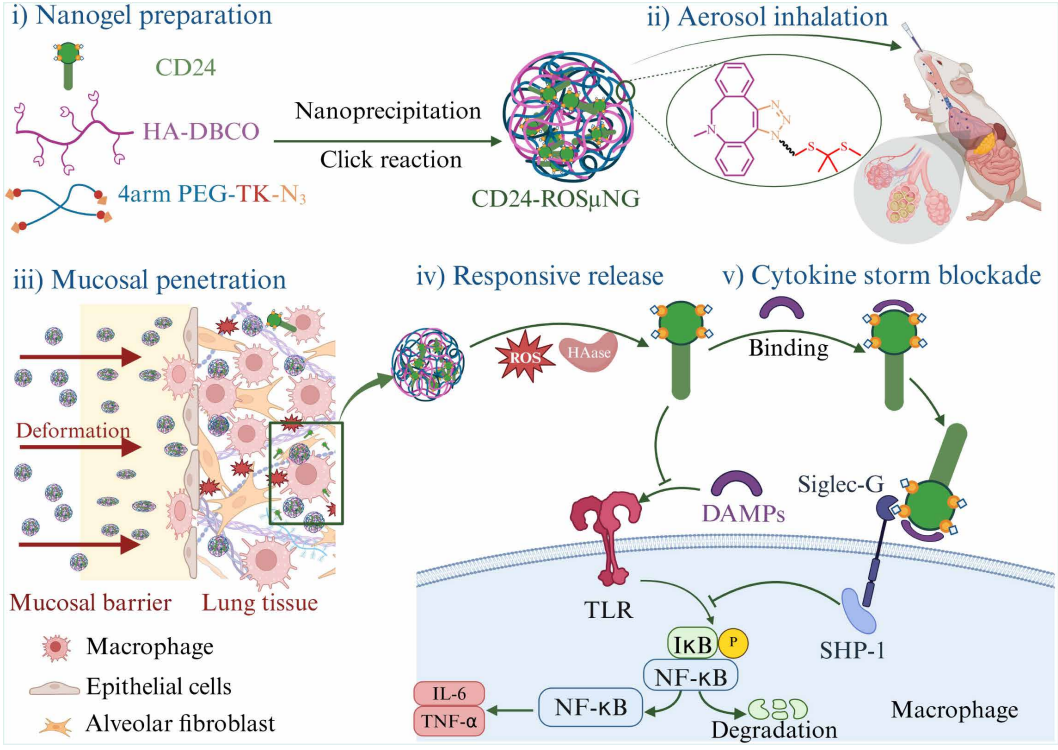

Fig. 1. Construction of inhalable ROSμNG for pulmonary CD24 delivery to rescue acute pneumonia by selective inhibition of hyperinflammatory response. ROSμNG fabricated via a copper-free click reaction between HA-DBCO and 4arm PEG-TK-N_3 displayed high stability against nebulization, transformability for efficient mucosal penetration, and triggered CD24 release, leading to significant blockade of cytokine storm, suppression of DAMP-mediated inflammation, and survival extension. Created in BioRender. Sun, Y. (2026) https://BioRender.com/ngczd8i.

nebulization-induced inactivation while remaining responsive to the heightened oxidative environment of inflamed lungs. PEGylation and transformability enhance mucus penetration and ensure uniform alveolar distribution (*24*–*27*), whereas thioketal linkages undergo cleavage in the presence of ROS, thereby enabling controlled release precisely at sites of inflammation (*28*–*30*). CD24 serving as a phagocytosis checkpoint has been implicated in tumor progression, invasion, and metastasis, spurring substantial research interest in cancer treatment (*31*, *32*). Moreover, growing evidence reveals vital roles of CD24 in diverse pathological settings including autoimmune dysregulation, metabolic disorders, inflammatory cascades, and graft-versus-host diseases (*33*). In preclinical models, CD24-loaded ROSμNG achieved high pulmonary retention, suppressed cytokine storm, attenuated lung injury, and significantly improved survival in lipopolysaccharide (LPS)–induced pneumonia. In H1N1 influenza models, the formulation resolved the conflict between inflammation suppression and immune defense by simultaneously controlling hyperinflammation and preserving neutrophil-mediated antiviral activity. Together, these findings establish inhalable CD24 nanogels as a promising therapeutic strategy to resolve pulmonary hyperinflammation without undermining essential host immunity.

RESULTS AND DISCUSSION

ROSμNG preparation

ROSμNG was constructed from HA-DBCO and 4arm PEG-TK-N_3 by combining click chemistry and nanoprecipitation. HA-DBCO was synthesized via amidation reaction of HA with DBCO-NH_2 (fig. S1), and the characteristic aromatic ring signals in ^{1}H nuclear magnetic resonance (NMR) spectrum [7.0 to 7.6 parts per million (ppm)] and a distinct absorption band at 750 and 1550 cm^{-1} in Fourier transform infrared (FTIR) spectrum confirmed the successful conjugation (fig. S2A). The degree of substitution (DS), defined as the number of functional groups per 100 HA sugar residues, was determined to be 12.5 by integrating characteristic proton signals (—CH_3 of HA, 1.5 to 1.9 ppm; —C_6H_4 of DBCO, 7.0 to 7.6 ppm) in the ^{1}H NMR spectrum (fig. S2B). The synthesis of 4arm PEG-TK-N_3 involved a sequential amidation reaction of 4arm PEG-NH_2 with excess TK-containing dicarboxylic acid and 3-azido-1-propylamine (fig. S3). FTIR analysis revealed characteristic azide stretching at 2100 cm^{-1} and PEG backbone C—O—C vibration at 1100 cm^{-1} (fig. S4A). Structural characterization of 4arm PEG-TK-N_3 was further performed using ^{1}H NMR spectrum, where integration of characteristic proton signals from the TK methyl (—CH_3, 1.6 ppm), 3-azido-1-propylamine methylene (—CH_2, 3.38 ppm), and PEG methylene (—OCH_2CH_2—, 3.6 ppm) confirmed an azide DS value of 3.9 (fig. S4B). In a similar way, nonresponsive nanogels (μNGs; TK^-/PEG^+) derived from HA-DBCO and 4arm PEG-N_3, as well as nonresponsive/PEGylated nanogels (NGs; TK^-/PEG^-) developed from HA-DBCO and HA-N_3, served as controls in exploring the influence of PEG and TK moieties on nanogel properties. HA-N_3 with a DS of 17.5 was synthesized via amidation between 3-azido-1-propanamine and HA (fig. S5), and the structure was verified by the characteristic proton signals in the ^{1}H NMR spectrum (—$NHCH_2$— of 3-azido-1-propanamine, 3.1 ppm; —CH_3 of HA, 1.8 to 2.1 ppm) and a distinct absorption band at 2100 cm^{-1} (azido

group) in FTIR spectrum (fig. S6). Matrix-assisted laser desorption/ionization–time-of-flight mass spectrometry revealed that the main mass/charge ratio (m/z) shifts from 5025 for 4arm PEG-NH_2 to 6266 for 4arm PEG-TK-N_3 (fig. S7A). The observed $\Delta m/z$ of 1241 corresponds to the theoretical value of 1264 minus Na^+ adduct, confirming the successful synthesis and structural integrity of PEG-TK-N_3. In addition, gel permeation chromatography (GPC) measurement determined the molecular weights of HA, HA-N_3, and HA-DBCO as 36.5, 38.4, and 42.6 kDa, respectively, (fig. S7B), indicating the successful synthesis of these derivatives.

The cross-linking of ROSμNG via click chemistry was monitored by ultraviolet-visible (UV-Vis) and FTIR spectroscopy. The disappearance of the absorption peaks at 290 nm (azide group) and 308 nm (DBCO) in the UV-Vis spectra, along with the absence of azide characteristic signal at 2100 cm^{-1} in the FTIR spectrum, corroborated that the click reaction was complete (fig. S8). ROSμNG displayed a hydrodynamic diameter of 183 nm [polydispersity index (PDI) = 0.13], a zeta potential of −21.6 mV (table S1), and remarkable CD24 loading capacity, showing a protein loading efficiency (PLE) exceeding 95% at theoretical protein loading contents (PLCs) up to 25 wt % (Fig. 2A). CD24-ROSμNG at a PLC of 24.4 wt % presented a slightly increased size of 190 nm (PDI < 0.2) and negative zeta potential of −20.8 mV. TEM further corroborated the spherical morphology with narrow size distribution (Fig. 2B and fig. S9). Besides CD24, ROSμNG revealed efficient encapsulation of diverse proteins spanning molecular weights of 12 kDa (cytochrome c) to 250 kDa (catalase) with encapsulation efficiencies exceeding 70% (table S1), indicating its potential as a universal platform for protein delivery. The protein-loading capacity of ROSμNG was markedly impaired by NaCl and urea (fig. S10), signifying that the loading process was predominantly mediated by hydrogen bonding and electrostatic attraction between HA and the proteins. Notably, protein-loaded ROSμNG demonstrated exceptional stability, exhibiting negligible size change under high-shear nebulization, extended storage (28 days, 4°C), and exposure to biological fluids [10% fetal bovine serum (FBS), 4 hours] (Fig. 2C and fig. S11). Besides, minimal drug leakage from ROSμNG was observed following nebulization and long-term storage (fig. S12). The remarkable stability is mainly attributed to synergistic effects of covalent cross-linking via DBCO-azide click chemistry forming a robust nanogel network and surface charge-driven electrostatic repulsion verified by pronounced aggregation of ROSμNG upon NaCl addition (fig. S13).

During pulmonary delivery of bioactive drugs, such as proteins and nucleic acids, preserving their structural and functional integrity remains a paramount challenge (*34*, *35*). Notably, CD24 loaded in nanogel formulations (NG, μNG, and ROSμNG) maintained >90% bioactivity postnebulization, while the free protein suffered more than 25% activity loss (Fig. 2D). Following 2-hour treatment with trypsin (0.1%) at 37°C, CD24 loaded in nanogels retained 75% residual activity compared to merely 28% for native CD24, signifying remarkable protein protection by nanogels. To explore pulmonary delivery potential, a 1.5-mm-thick artificial mucus model was developed (Fig. 2E) according to a previous report (*36*). Fluorescence analysis demonstrated that both ROSμNG (TK^+/PEG^+) and μNG (TK^-/PEG^+) achieved rapid mucus penetration within 1 hour, showing more than 15-fold higher fluorescence intensities in the lower chambers compared to the NG group (TK^-/PEG^-) at 4 hours (Fig. 2, F and G). In murine pneumonia models, fluorescence imaging of lung sections revealed that both μNG and ROSμNG induced homogeneous distribution of CD24-Cy5 throughout the lung parenchyma within 1 hour postnebulization (Fig. 2H), further signifying fast mucus traversal and effective protein delivery. In contrast, NG without PEG resulted in minimal mucus penetration, showing substantial protein aggregation in bronchial areas. These findings underscore the critical role of PEGylation in overcoming mucoadhesion through dual mechanisms of hydration layer formation and electrostatic shielding, consistent with previous studies for PEGylated nanoparticles (*37*). Liquid-phase atomic force microscopy (AFM) was used to characterize the mechanical properties of nanogels. Analysis of force-displacement curves revealed that the Young's modulus of CD24-ROSμNG closely matched that of lung mucus (Fig. 2I), suggesting their structural adaptability to deform and effectively traverse the mucin network (*26*). Cryo–scanning electron microscopy (cryo-SEM) further demonstrated pronounced morphological reshaping of ROSμNG as they navigated through the pore structures of artificial mucus (Fig. 2, J and K).

To validate ROS responsiveness, we treated ROSμNG with different concentrations of H_2O_2 (0.1 to 10 mM) and found a heterogeneous size distribution accompanied by substantial size enlargement after 12 hours (fig. S14). The structural dissociation was mainly attributed to TK bond cleavage, as verified by the gradual attenuation of the characteristic TK methyl proton signal at 1.60 ppm in 4arm PEG-TK-N_3 with escalating H_2O_2 concentrations (fig. S15). TK enables ROS-triggered degradation through selective cleavage of carbon-sulfur bonds under oxidative conditions, and has been incorporated to develop varying ROS-responsive drug carriers. As expected, ROSμNG displayed H_2O_2 concentration–dependent CD24 release profiles (Fig. 2L). Under simulated pneumonia microenvironment conditions [0.1 mM H_2O_2 + 10 U/ml hyaluronidase (HAase)] (*38*, *39*), the release kinetics accelerated significantly due to HAase-mediated degradation and H_2O_2-triggered TK cleavage, achieving 90% protein release within 36 hours (Fig. 2M and fig. S16). Circular dichroism (CD) measurement revealed that the released CD24 maintained a secondary structure identical to that of the native protein, while enzyme-linked immunosorbent assay (ELISA) quantification demonstrated that over 95% of the binding capacity to Siglec-G was retained (fig. S17), corroborating the maintenance of protein structure and bioactivity throughout the nanogel preparation processes. In bronchoalveolar lavage fluid (BALF) collected from LPS-infected mice, over 85% of the protein activity was preserved for CD24 released from ROSμNG within 24 hours (fig. S18), indicating the maintenance of CD24 activity in the inflamed lung tissues for therapeutic applications.

In vitro anti-inflammatory effect of CD24-ROSμNG

Macrophages represent the frontline immune defense in pneumonia pathogenesis, serving as pivotal regulators in both initiating and maintaining inflammatory responses by providing ROS and proinflammatory cytokines (*40*–*42*). In LPS-stimulated RAW264.7 macrophages, CD24-ROSμNG exhibited significant anti-inflammatory regulatory effects in the presence of DAMPs [e.g., high mobility group box 1 (HMGB-1)] with around 50% reduction in interleukin-6 (IL-6) production and substantial elevation of IL-10 expression, outperforming CD24-NG and CD24-μNG groups (Fig. 3, A and B). Excess ROS levels are known to cause substantial tissue damage and exacerbate inflammatory cascades in acute pneumonia, making the modulation of ROS homeostasis a valuable therapeutic target for severe cases (*43*). RAW264.7 macrophages stimulated by LPS

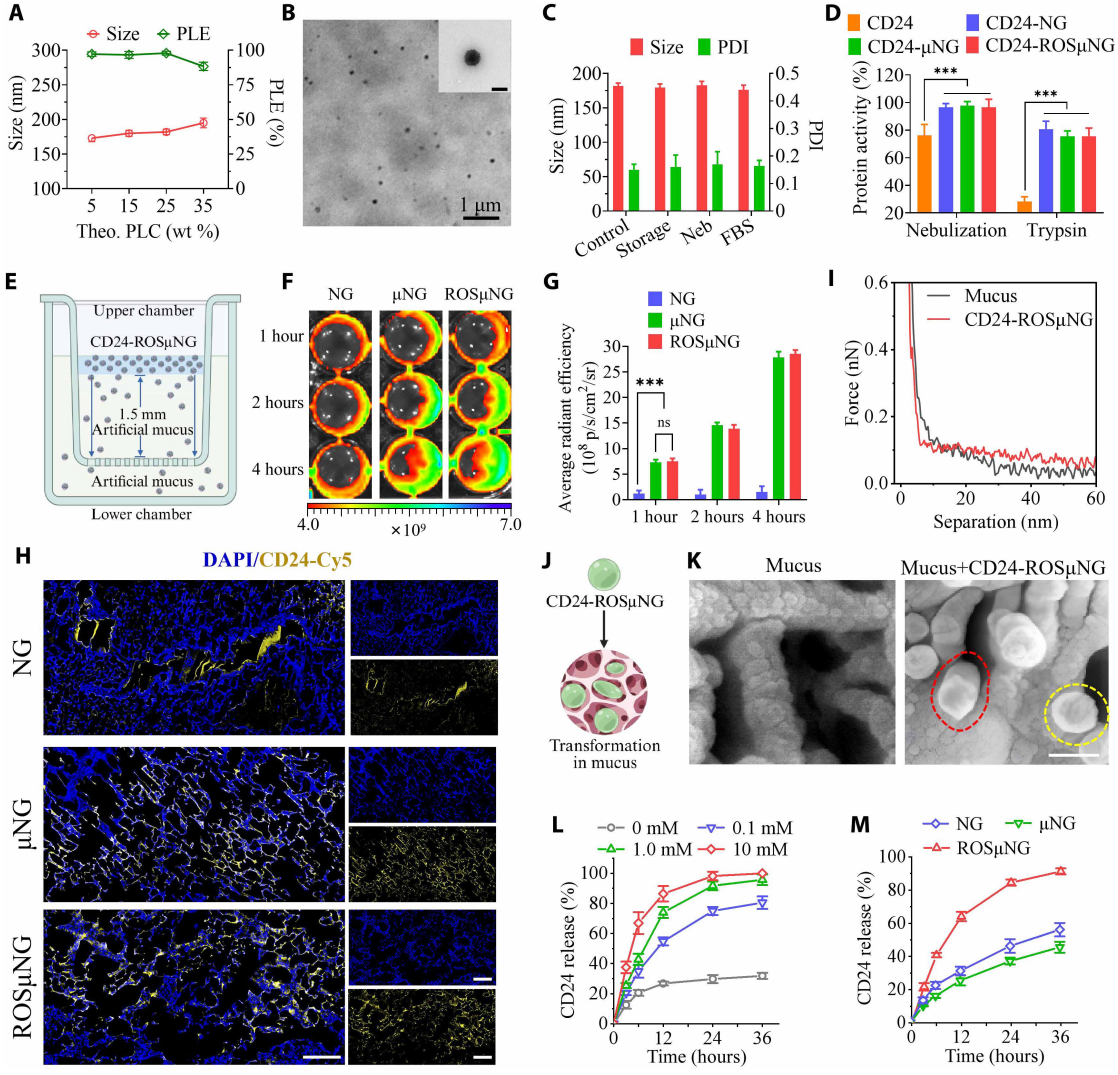

Fig. 2. Characterizations of CD24-ROSμNG. (**A**) Size and PLE at varying theoretical CD24 PLC (Theo. PLC) ($n = 3$). (**B**) TEM images at a PLC of 24.4 wt %. Scale bars, 1.0 μm (main panel) and 200 nm (inset). (**C**) Stability of CD24-ROSμNG against Neb (nebulization), long-term storage (28 days, 4°C), and 10% FBS (37°C) ($n = 3$). (**D**) Residual activity of CD24 following nebulization and trypsin treatment ($n = 3$). (**E**) Schematic illustration of an in vitro mucus penetration assay within an artificial mucus layer. (**F**) Fluorescence microscopy images of the lower chamber demonstrating nanogel penetration through a simulated mucus layer in a transwell migration assay. (**G**) Semiquantification of fluorescence intensity ($n = 3$). (**H**) Representative images of CD24 lung enrichment in the LPS-induced acute pneumonia model following nebulization administration of nanogels loaded with CD24 (CD24: 1.5 mg/kg). Lung tissue harvested 1 hour postadministration was stained with DAPI (blue, nuclei). CD24 was labeled with Cy5 (yellow). Scale bars, 100 μm. (**I**) Force-separation curves of CD24-ROSμNG and artificial mucus. (**J**) Schematic diagram of the deformation of nanogels while traversing mucin networks. (**K**) Sectional view illustrating the deformation of ROSμNG as it passes through mucin microporous membrane observed by cryo-SEM. The areas demarcated by red and yellow dotted lines indicate the deformed and normal CD24-ROSμNG, respectively. Scale bar, 200 nm. (**L**) In vitro CD24 release profiles from ROSμNG at different H_2O_2 concentrations ($n = 3$). (**M**) In vitro CD24 release profiles from NG, μNG, or ROSμNG in the presence of 0.1 mM H_2O_2 and 10 U/ml HAase ($n = 3$).

displayed significantly elevated ROS production as evidenced by intense green fluorescence under 2′,7′-Dichlorodihydrofluorescein diacetate (DCFH-DA) staining (Fig. 3C). The augmented ROS in the cells was remarkably attenuated by CD24-ROSμNG, affording approximately threefold less ROS levels compared to the phosphate-buffered saline (PBS) group (Fig. 3D). ROSμNG vector exhibited concentration-dependent ROS scavenging efficacy, showing little ROS elimination at its concentration in CD24-ROSμNG formulation (0.5 μg/ml) while significant ROS scavenging upon increasing the concentration to 5.0 μg/ml. The inherent antioxidant capacity of ROSμNG was further verified by its H_2O_2 decomposition performance at concentrations of 0.5 to 2.0 mg/ml (fig. S19).

The DAMP-associated immunomodulation mechanism of CD24-ROSμNG was explored in LPS-activated RAW264.7 macrophages. With increasing HMGB-1 concentrations, CD24-ROSμNG induced a gradual reduction of proinflammatory cytokines like IL-6 (Fig. 3E). This suppression was attributed to enhanced Siglec-G pathway activation driven by elevating generation of HMGB-1–CD24 complexes. Through binding to DAMPs such as HMGB-1, CD24 blocks their pro-inflammatory signaling and concurrently activates the downstream

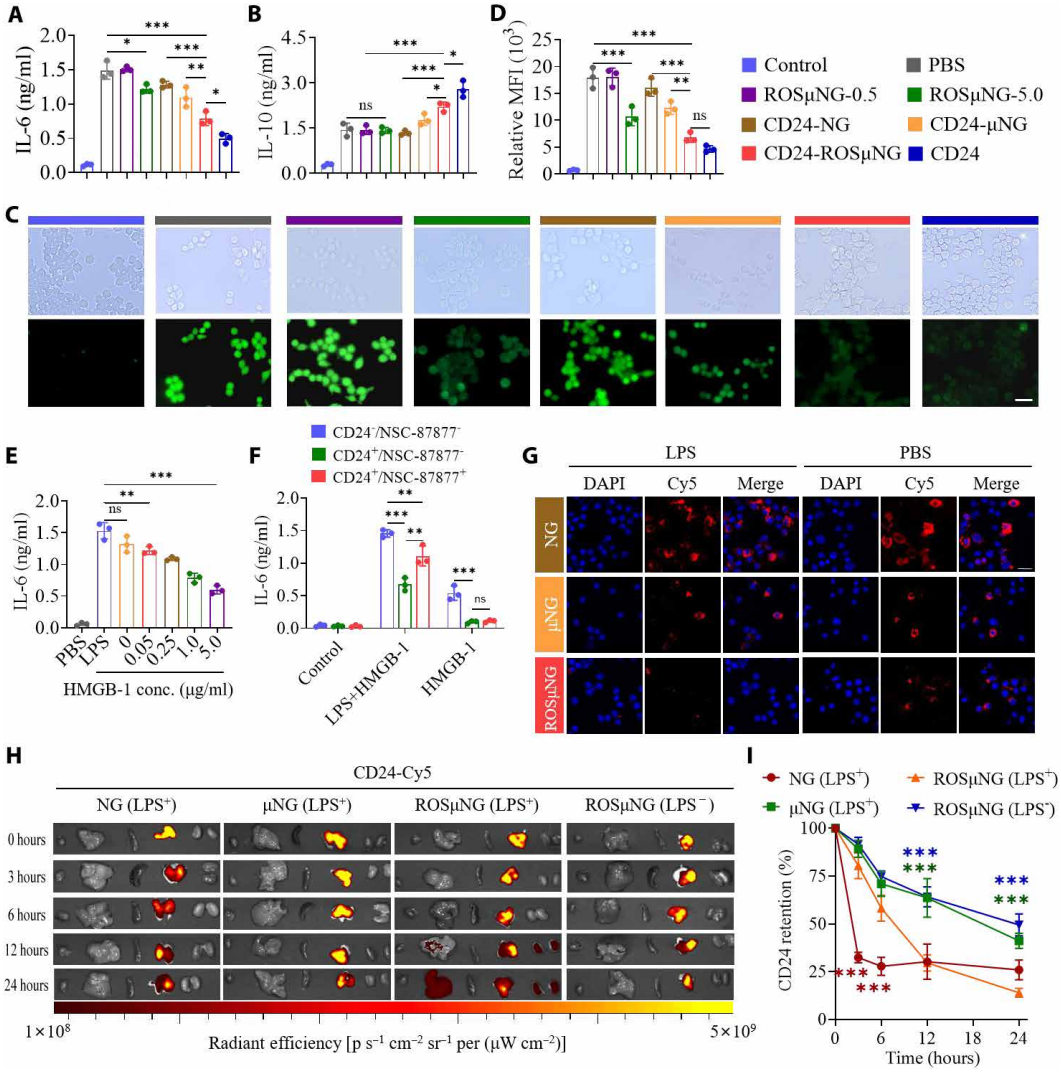

Fig. 3. In vitro anti-inflammatory effect and pulmonary enrichment. In the LPS-treated group, RAW264.7 cells were treated with LPS at 1.0 μg/ml for 1 hour prior to incubating with CD24-loaded nanogels. The secretion levels of IL-6 (**A**) and IL-10 (**B**) by LPS-treated RAW264.7 cells following the treatment with PBS, ROSμNG-0.5 (0.5 μg/ml), ROSμNG-5.0 (5.0 μg/ml), CD24-NG, CD24-μNG, CD24-ROSμNG, or free CD24, along with HMGB-1 (5.0 μg/ml) ($n = 3$). CD24 concentration was fixed at 150 ng/ml. (**C**) Representative images of intracellular ROS generation in RAW264.7 cells. ROS was visualized by staining with DCFH-DA (green, 10 μM) for 30 min. Scale bar, 20 μm. (**D**) Relative mean fluorescence intensity (MFI) of DCFH-DA–stained ROS ($n = 3$). (**E**) HMGB-1 concentration correlation of CD24-ROSμNG (CD24: 300 ng/ml) anti-inflammatory capacity ($n = 3$). (**F**) Validation of the action mechanism of CD24 by SHP-1 inhibitor (NSC-87877) ($n = 3$). RAW264.7 cells were treated with NSC-87877 (10 μM) for 2 hours and then stimulated with LPS (1 μg/ml), HMGB-1 (5 μg/ml), or their combination (as a positive control), followed by incubation with CD24-ROSμNG (CD24: 300 ng/ml) for 24 hours. (**G**) CLSM images of RAW264.7 cells treated with CD24-loaded nanogels for 4 hours. CD24 was labeled with Cy5 (red), and nuclei were stained with DAPI (blue). Scale bar, 20 μm. (**H**) Ex vivo fluorescence imaging of CD24-Cy5 in major organs via IVIS after inhalation administration with different formulations. In each group, the organs from left to right were heart, liver, spleen, lung, and kidney. (**I**) Quantitative average fluorescence intensity of CD24-Cy5 in the lung tissues ($n = 3$). Statistical analyses for differences shown in the figure were all conducted using ROSμNG (LPS^+) group as the reference. $^*P < 0.05$; $^{**}P < 0.01$; $^{***}P < 0.001$; ns, not significantly different at $P > 0.05$.

immunosuppressive Siglec-G pathway, thereby achieving selective suppression of inflammatory immunity (*44*). NSC-87877, an SHP-1 inhibitor to block CD24–Siglec-G–mediated suppression of NF-κB activation (*45*, *46*), was used to investigate the role of CD24-DAMP interaction in inflammation control. Following stimulation with LPS and HMGB-1, NSC-87877 induced a smaller reduction in IL-6 in RAW264.7 cells compared to non–NSC87877-treated group (Fig. 3F), indicating that CD24-mediated activation of the Siglec-G signaling pathway is essential for immunomodulation. In DAMP–CD24–Siglec-G axis, CD24 activates the Siglec-G signaling pathway by binding DAMPs to form a binary complex, triggering downstream production of SHP-1 phosphatase to inhibit NF-κB–mediated inflammatory cascades (fig. S20). In comparison with untreated group ($CD24^-$/$NSC\text{-}87877^-$), macrophages treated with NSC-87877 and CD24-ROSμNG ($CD24^+$/$NSC\text{-}87877^+$) displayed lower IL-6 levels, suggesting that besides Siglec-G signaling axis, CD24 might mediate immunomodulatory effects through alternative mechanisms like Toll-like receptor 4 (TLR4) pathway modulation and physical sequestration of

DAMPs (*15*, *16*). In addition, CD24-ROSμNG revealed significant anti-inflammatory efficacy with comparable IL-6 concentration in HMGB-1–stimulated RAW264.7 cells after treatment with NSC-87877, further verifying an alternative signaling pathway other than Siglec-G axis for immunomodulation. Western blot analysis revealed that CD24-ROSμNG treatment potently suppressed NF-κB activation in LPS-stimulated RAW264.7, as evidenced by inhibited degradation of IκBα and a marked reduction in the phosphorylation level of the transcription factor p65 (p-p65; fig. S21). These results provide pathway-specific biochemical evidence that CD24 directly modulates inflammatory signaling rather than merely producing phenotypic anti-inflammatory effects.

Considering that CD24 targets Siglec-G receptors on the cell surface, extracellular protein release is crucial for therapeutic optimization. In LPS-treated and untreated RAW264.7 cells, both ROSμNG and μNG formulations demonstrated markedly lower cellular uptake compared to NG (Fig. 3G and figs. S22 and S23), highlighting the essential role of PEGylation in maximizing the interaction of loaded CD24 with Siglec-G on the cell surface. Notably, ROSμNG showed a 35% reduction in protein internalization compared to μNG group in RAW264.7 cells stimulated with LPS for 4 hours, attributable to its ROS-responsive extracellular payload release. Flow cytometry analysis further confirmed ROS-triggered extracellular protein retention and PEGylation-mediated suppression of cellular uptake, as evidenced by a significant decrease in Cy5-positive cells. Thus, ROSμNG represents an advanced delivery platform for spatially controlled drug release in pulmonary applications. Cholecystokinin-8 (CCK-8) assays revealed that RAW264.7 cells treated with CD24-ROSμNG exhibited a cell viability exceeding 95% (fig. S24), verifying their exceptional cytocompatibility.

In vivo distribution and biosafety of CD24-ROSμNG

Compared to conventional oral and intravenous administration routes, pulmonary delivery enables direct targeting with enhanced drug bioavailability, offering a promising therapeutic strategy for pneumonia management (*47*–*49*). However, pathological mucus hypersecretion imposes a critical barrier to nanocarrier penetration (*50*, *51*). To investigate pulmonary retention profiles, CD24 conjugated with Cy5 (CD24-Cy5) was loaded in Cy7-labeled nanogels for dual-channel tracking. Following pulmonary administration via nebulization in a murine acute pneumonia model, CD24 exhibited predominant pulmonary accumulation with minimal off-target signals detected in other organs (lung, liver, spleen, heart, and kidney) (Fig. 3H). In contrast with rapid CD24 signal attenuation in the NG group, μNG and ROSμNG retained >80% initial signal intensity 3 hours after administration (Fig. 3I), aligning with mucus penetration performance. Over time, the ROSμNG group displayed accelerated CD24 signal decline in inflamed lungs versus μNG, correlating with inflammation-driven protein release (Fig. 2I). Compared to CD24 protein, nanogels displayed similar signal deposition and decay in major organs (fig. S25), underscoring the therapeutic potential for pulmonary inflammation. Biodistribution analysis revealed that both μNG and ROSμNG achieved lung-targeted enrichment of CD24 protein, demonstrating over 80% of the protein accumulated in the lung tissues in both healthy mice and LPS-induced inflammatory models within 3 hours postnebulization (fig. S26). In contrast, minimal CD24 distribution was detected in other major organs, verifying negligible off-target drug accumulation. To investigate the in vivo drug release and pharmacokinetics of different formulations, free CD24 concentrations in both BALF and serum of mice were measured at designated time points using an ELISA kit. Following inhalation administration in mice with pneumonia, CD24-ROSμNG group displayed a fast increase of CD24 concentration (16.3 μg/ml) in the BALF at 6 hours postadministration, which was twofold higher than the nonresponsive counterpart group (CD24-μNG) (fig. S27A). Moreover, both CD24-ROSμNG and CD24-μNG revealed low and comparable CD24 levels in BALF of healthy mice throughout the study, confirming ROS-triggered drug release. The protein concentrations in serum showed corresponding changes correlated with alterations in pulmonary status (fig. S27B).

To evaluate the long-term biosafety of CD24-ROSμNG, we conducted comprehensive monitoring in healthy mice over a 28-day period postadministration. Hematoxylin and eosin (H&E)–stained organs confirmed formulation safety, with all treatment groups exhibiting intact tissue architecture and absence of cytotoxicity (fig. S28). Using comparative analysis with healthy mice, the treatment group revealed comparable levels of biochemical [e.g., alanine aminotransferase (ALT), aspartate aminotransferase (AST), and creatinine (CREA)] and hematological [e.g., white blood cell (WBC), red blood cell (RBC), and platelet (PLT)] parameters from day 7 to day 28 (fig. S29A), signifying negligible adverse effects on hepatorenal function, systemic inflammation responses, and hematopoietic systems. Moreover, malondialdehyde (MDA) level assessments indicated that CD24-ROSμNG did not disrupt ROS homeostasis in treated mice, preserving essential redox signaling and related metabolic processes (fig. S29B). These cumulative findings substantiate that CD24-ROSμNG has excellent biocompatibility and systemic safety for long-term in vivo therapeutic applications.

CD24-ROSμNG rescues acute pneumonia

A murine acute pneumonia model was established via laryngotracheal LPS instillation (40 mg/kg) to assess in vivo therapeutic efficacy (Fig. 4A). After 2 hours, the mice received different formulations once a day for three consecutive days. H&E staining revealed that mice treated with CD24-ROSμNG demonstrated nearly intact lung structure with slight alveolar wall thickening (Fig. 4B). Lung injury scores based on a four-tier grading system approached normal values in the CD24-ROSμNG group, indicating minimal tissue damage (Fig. 4C). On the contrary, ROSμNG and CD24 + ROSμNG displayed minimal therapeutic effect as evidenced by severe alveolar collapse and structural disintegration similar to those observed in the PBS group. Notably, CD24-μNG showed weaker therapeutic effects compared to CD24-ROSμNG (Fig. 4B), highlighting the critical role of ROS-responsive drug release. Additional pulmonary function measurements demonstrated that mice treated with CD24-ROSμNG exhibited peripheral capillary oxygen saturation (SpO_2) and respiratory rate comparable to healthy controls (fig. S30), indicating minimal impairment of gas exchange. Compared to PBS group, BALF protein levels were significantly reduced in CD24-ROSμNG group (fig. S31), supporting a more intact alveolar-capillary barrier. The lung wet/dry (W/D) weight ratio, a typical indicator of endothelial-epithelial barrier dysfunction in acute pneumonia (*52*), revealed that ROSμNG + free CD24 presented comparable edema severity to the PBS group (Fig. 4D), suggesting that simple physical blending of CD24 with nanogels could not maintain the protein bioactivity during nebulization. Both CD24-μNG and CD24-ROSμNG significantly attenuated pulmonary edema. In addition, CD24-ROSμNG markedly decreased MDA levels (Fig. 4E), a key lipid peroxidation product that cross-links biomacromolecules to induce cytotoxicity (*53*, *54*).

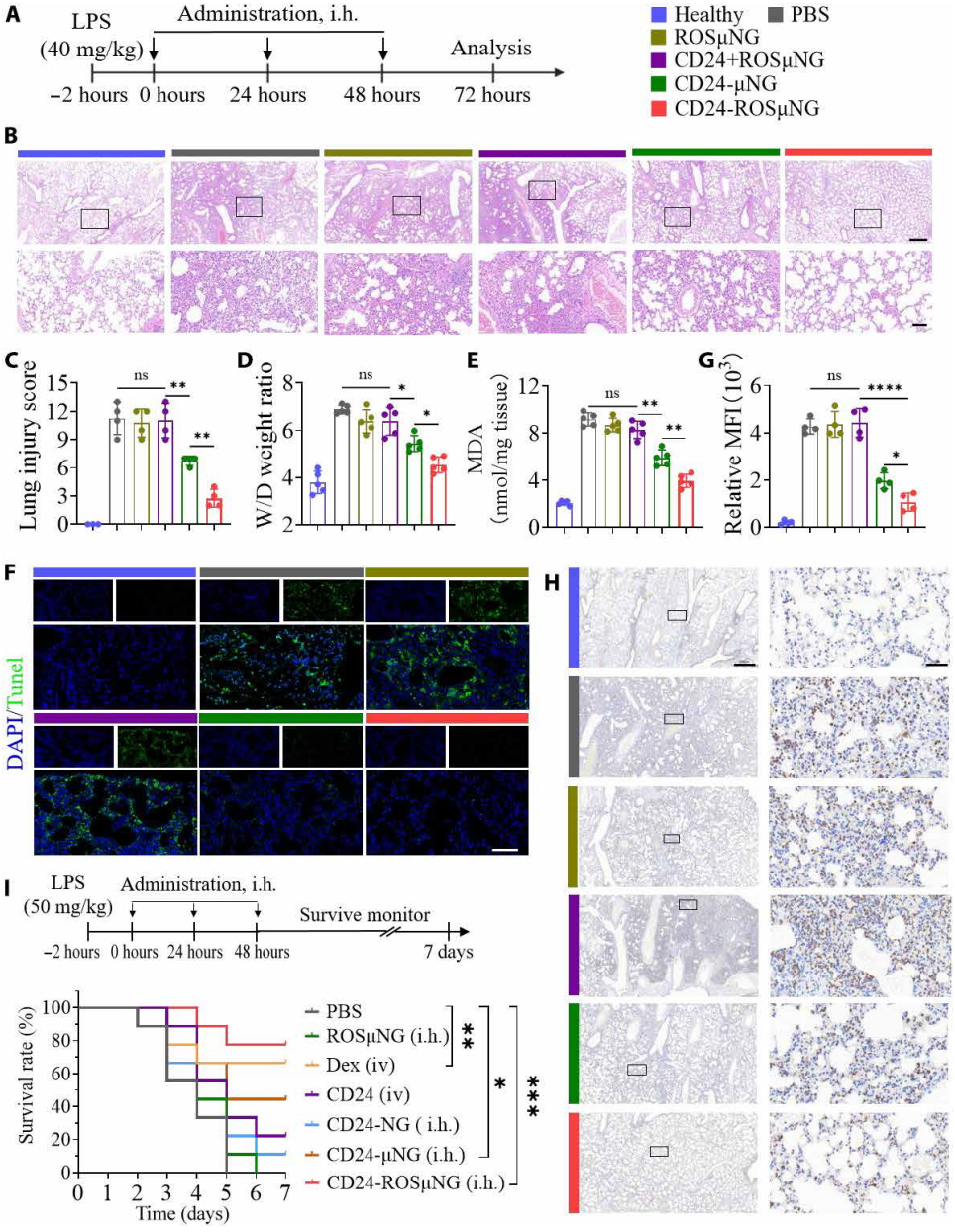

Fig. 4. In vivo therapeutic effect toward LPS-induced acute inflammation. (**A**) The treatment schedule for severe acute pneumonia established in Balb/c mice through intratracheal instillation of LPS (40 mg/kg) ($n = 6$). Nebulized treatments were given 2 hours post–LPS induction, with analysis 24 hours after the final dose. (**B**) Representative H&E staining of lung tissue. Bottom panels show magnified images at the locations indicated in the top panels. Scale bars, 500 and 100 μm for overview and magnified images, respectively ($n = 4$). (**C**) Lung injury scores assessed by a four-tier grading system ($n = 4$). (**D**) W/D weight ratio ($n = 5$). (**E**) MDA levels ($n = 5$). (**F**) Representative images and (**G**) quantitative analysis of cell apoptosis in lung tissue after being stained with DAPI (blue, nuclei) and Tunel reaction solution (green, apoptotic cells) ($n = 4$). Scale bar, 200 μm. (**H**) Representative images of MPO in the lung tissues. The magnified images at the positions pointed out are shown on the right. Blue, nuclei; brown, MPO-positive cells. Scale bars, 500 and 50 μm for the overview and magnified images, respectively. (**I**) Therapeutic evaluation for lethal acute pneumonia in Balb/c mice established through intratracheal drops of LPS (50 mg/kg) ($n = 9$). Two hours postinduction, the mice were treated once daily for three consecutive days with PBS, ROSμNG [6.0 mg/kg, inhalation (i.h.)], Dex (1.5 mg/kg, iv), CD24-NG (CD24: 1.5 mg/kg, i.h.), CD24-μNG (CD24: 1.5 mg/kg, i.h.), or CD24-ROSμNG (CD24: 1.5 mg/kg, i.h.). A single intravenous injection of CD24 (55.0 mg/kg) served as a control. H&E and MPO staining were performed on sequential histological sections derived from identical lung tissue samples. *$P < 0.05$; **$P < 0.01$; ***$P < 0.001$; ****$P < 0.0001$; ns, not significantly different at $P > 0.05$.

This reduction correlated with mitigated ROS-mediated damage to alveolar epithelial and endothelial cells. Tunel assay revealed that CD24-ROSμNG significantly suppressed inflammation-associated apoptosis, showing apoptosis levels close to healthy mice (Fig. 4, F and G). Although CD24-ROSμNG treatment induced a significant increase in neutrophil levels at 24 hours, the neutrophils rapidly returned to near normal levels by 48 hours after the last administration (fig. S32). Myeloperoxidase (MPO) activity, indicative of neutrophil-mediated oxidative injury (*55*), was substantially reduced by CD24-μNG and CD24-ROSμNG (Fig. 4H), suggesting that the transient increase in neutrophils cause insignificant tissue damage. Notably, CD24-ROSμNG demonstrated progressive alleviation of lung tissue injury and pulmonary edema, accompanied by reduced cell apoptosis caused by inflammatory stimuli as CD24 dosage increased from 0.25 to 1.50 mg/kg (fig. S33).

To assess the rescue efficacy in acute pneumonia, we further established a lethal murine model via laryngotracheal LPS instillation (50 mg/kg), as previously reported (*38*). PBS-treated mice exhibited initial mortality on day 2, with complete lethality by day 5 (Fig. 4I). CD24 nanogels exhibited marked therapeutic efficacy, and CD24-NG, CD24-μNG, and CD24-ROSμNG afforded survival rates of 11.1, 44.4, and 77.8%, respectively. Compared to intravenous administration of free drug at a 12-fold higher dose [55.0 mg/kg, as per the clinical study; (*17*)], CD24-ROSμNG demonstrated over 3.5-fold increase in survival rate, attributable to enhanced drug utilization and pulmonary targeting administration. Corticosteroid therapy (e.g., Dex), although demonstrating significant therapeutic effects, afforded a lower survival rate in comparison with CD24-ROSμNG, underscoring the potential of CD24-ROSμNG as a promising candidate for severe pneumonia management. The long-term safety and efficacy of CD24-ROSμNG were evaluated through comprehensive histological examination at 1 week and 1 month posttreatment. H&E staining demonstrated well-preserved pulmonary architecture with minimal tissue structural disruption in CD24-ROSμNG–treated mice at both time points (fig. S34A), confirming sustained therapeutic benefits. Masson staining revealed negligible collagen deposit in lung tissues, indicating effective mitigation of fibrotic progression. These findings hold particular clinical relevance given that persistent inflammatory damage and aberrant fibrotic remodeling constitute major determinants of respiratory dysfunction and long-term morbidity in severe pneumonia cases (*6*, *56*). Besides, mice following a 1-month treatment with CD24-ROSμNG exhibited hematological and biochemical parameters comparable to those of healthy mice (fig. S34B), indicating normal systemic inflammation levels, preserved hematopoietic activity, and maintained liver and kidney function. Different from established nanoplatforms such as lipid nanoparticles (LNPs) for intracellular nucleic acid delivery and poly(lactic-*co*-glycolic acid) nanoparticles (PLGA NPs) serving as sustained-release carriers for peptides and proteins (*57*–*60*), covalently cross-linked ROSμNG featured with structural robustness, enhanced mucus penetration capability, preserved protein bioactivity, and ROS-triggered drug release enables efficient pulmonary protein delivery and holds significant translational potential to manage pulmonary diseases.

Immunomodulation of CD24-ROSμNG in acute pneumonia

The predominant clinical challenges in severe acute pneumonia stem from cytokine storm syndrome, a life-threatening condition characterized by immune hyperactivation that drives excessive immune cell recruitment and cytokine production, leading to amplified inflammatory responses and multiorgan damage (*61*, *62*). Mice treated with empty ROSμNG and CD24 + ROSμNG displayed comparable cytokine levels and macrophage levels to the PBS group, showing negligible immunomodulation (Fig. 5, A to G). CD24-ROSμNG administration induced significant immunomodulation in murine models, exhibiting 50 to 70% reduction in the concentrations of proinflammatory mediators [IL-1β, IL-6, tumor necrosis factor–α (TNF-α), and interferon-γ (IFN-γ)] and twofold elevation of anti-inflammatory IL-10 level compared to the PBS group (Fig. 5, A to E, and fig. S35). This coordinated cytokine shift reflects observed improvements in histopathological indicators. Serum analysis revealed parallel immunomodulation with more than 80% IL-6 reduction and sevenfold IL-10 increase (fig. S36). During the onset and development of acute pneumonia, systemic inflammatory responses often trigger life-threatening complications including sepsis and multiorgan failure (*63*). Flow cytometry analysis revealed that CD24-ROSμNG treatment significantly reduced pulmonary macrophage infiltration and had obvious dose dependence (Fig. 5, F to G, and figs. S37 and S38), thereby disrupting the self-perpetuating cycle involving continuous cytokine release and subsequent macrophage activation. CD24-ROSμNG induced dose-dependent decrease of proinflammatory cytokine levels and attenuated macrophage infiltration in the lung tissues (figs. S35 to S38).

Transcriptomic analysis delineated the mechanism by which CD24-ROSμNG reshaped the immune landscape in severe pneumonia. Principal components analysis (PCA) and heatmap clustering revealed distinct transcriptional profiles among healthy, LPS-induced, and CD24-ROSμNG treated groups (fig. S39), with dynamics shifting across disease progression (days 1 and 3) and therapeutic intervention (Fig. 5, H to K). Kyoto Encyclopedia of Genes and Genomes (KEGG) pathway analysis revealed that LPS stimulation induced significant up-regulation of genes associated with core inflammatory signaling pathways spanning from Toll-like/NOD-like receptor activation to cytokine storm responses mediated by NF-κB/JAK-STAT signaling within 24 hours (fig. S40), illustrating the establishment of classic inflammatory responses in pneumonia. By day 3, the immune landscape shifted toward dysregulated inflammation, characterized by marked up-regulation of hyperinflammation pathways (e.g., complement/coagulation cascades linked to tissue injury) (fig. S41A) and down-regulation of adaptive immunity markers (e.g., allograft rejection and antiviral responses, signaling broad immune dysfunction) (fig. S41B). Thus, LPS administration induced acute inflammation within 24 hours in the murine pneumonia model, progressing to gradual immune exhaustion when the condition persisted beyond 3 days.

We analyzed differentially expressed genes (DEGs) at days 1 and 3 posttreatment in LPS-induced severe pneumonia models. Heatmap analysis revealed distinct expression patterns across time points (fig. S42). KEGG pathway and gene ontology (GO) enrichment demonstrated stage-specific immunomodulatory effects of CD24. On day 1, the treatment group maintained up-regulated cytokine-cytokine receptor interactions and concurrently suppressed TNF and IL-17 signaling pathways (Fig. 5, L and M), suggesting the maintenance of inflammatory immune activation and simultaneous containment of hyperinflammation and early-phase cytokine storm. GO analysis corroborated reduced leukocyte chemotaxis and myeloid leukocyte migration (fig. S43), confirming the inhibition of inflammatory cell recruitment. On day 3, CD24 treatment reversed the immune dysfunction. Up-regulation of allograft rejection

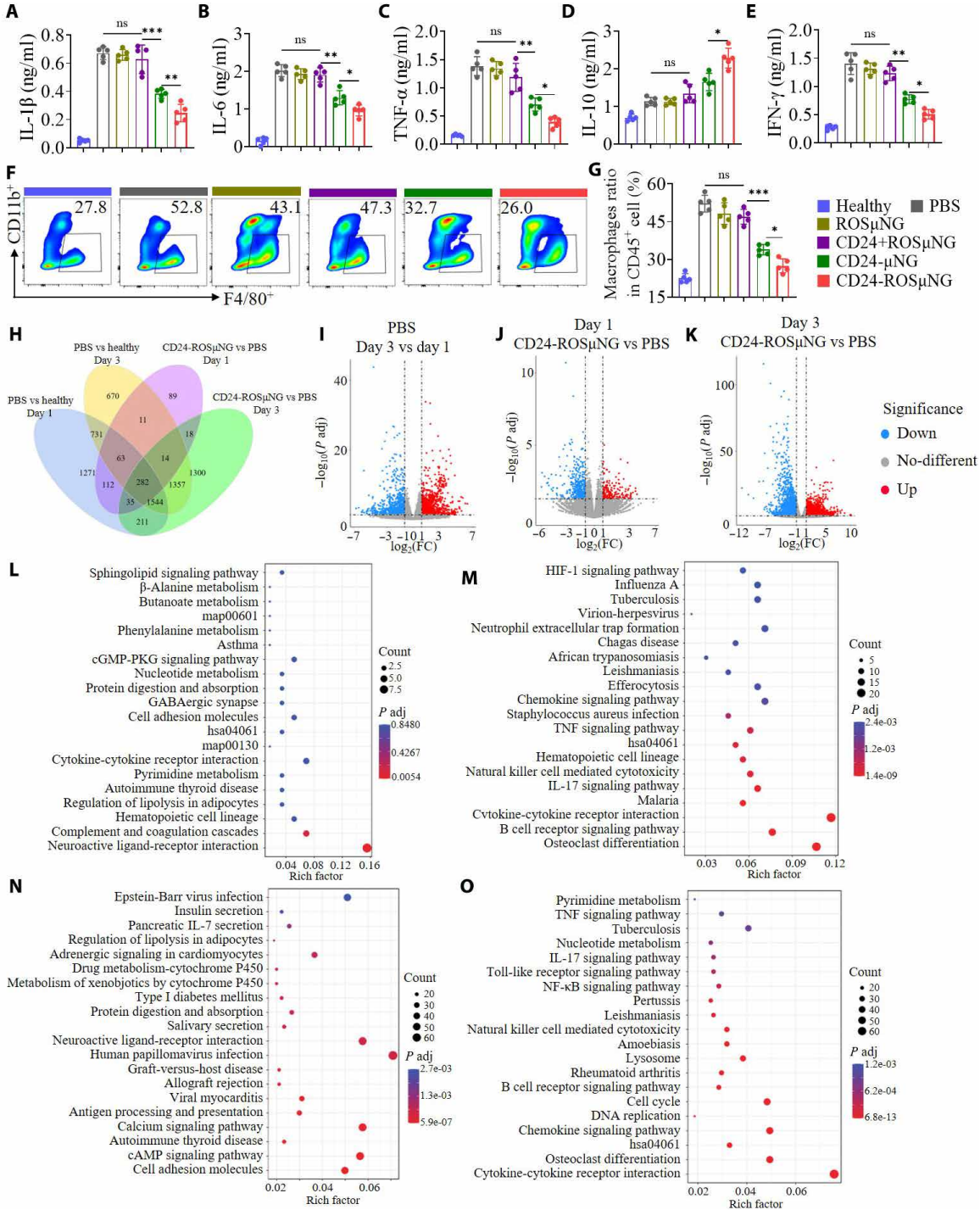

Fig. 5. Immunomodulation of the pulmonary inflammatory environments in LPS-induced severe pneumonia models. Levels of IL-1β (**A**), IL-6 (**B**), TNF-α (**C**), IFN-γ (**D**), and IL-10 (**E**) in the lung tissues following various treatments ($n = 5$). (**F**) Representative flow cytometry analysis graphs of $CD11b^{+lo}$ $F4/80^{+hi}$ cells in the total CD45 cell population. (**G**) Quantitative analysis of cell proportions ($n = 5$). (**H**) Venn diagram showing the number of DEGs in intersection of the comparison groups in PBS group (versus healthy group) and CD24-ROSμNG treatment group (versus PBS group) at different times (day 1 and day 3), $n = 3$. (**I**) Volcano plot in the PBS group on day 3 versus day 1, $n = 3$. Volcano plot in the CD24-ROSμNG group versus PBS group on day 1 (**J**) and day 3 (**K**), $n = 3$. KEGG pathway analysis of up-regulated (**L**) and down-regulated (**M**) DEGs in the lung tissues from CD24-ROSμNG versus PBS groups on day 1, $n = 3$. KEGG pathway analysis of up-regulated (**N**) and down-regulated (**O**) DEGs in the lung tissues from CD24-ROSμNG versus PBS groups on day 3, $n = 3$. The significantly enriched pathways are labeled with their official KEGG identifiers: Viral protein interaction with cytokine and cytokine receptor (hsa04061), glycosphingolipid biosynthesis-lacto and neolacto series (map00601), and ubiquinone and other terpenoid-quinone biosynthesis (map00130). Pathway identifiers are sourced from the KEGG database. $^{*}P < 0.05$; $^{**}P < 0.01$; $^{***}P < 0.001$; $^{****}P < 0.0001$; ns, not significantly different at $P > 0.05$.

pathways, antigen presentation, and B cell receptor signaling demonstrated revived T cell and humoral immune responses (Fig. 5N). Continued suppression of NF-κB, IL-17, and TNF pathways prevented persistent inflammation (Fig. 5O). Down-regulated GO terms further confirmed controlled immune hyperactivation across signaling initiation (e.g., pattern recognition receptor activity), cell recruitment (e.g., chemokine activity, granulocyte migration, and chemotaxis), and effector phase (e.g., cytokine activity and immune receptor activity) (fig. S44). These transcriptomic findings are functionally supported by pathway-level perturbation experiments. Pharmacological inhibition of SHP-1 partially abrogated the anti-inflammatory effects of CD24, indicating that the CD24–Siglec-G–SHP-1 axis is required for mediating the observed immunomodulatory effects. While we did not use genetic manipulation approaches in this study, the integration of pathway-specific biochemical validation, pharmacological perturbation, and time-resolved transcriptomic analyses establishes a coherent and biologically consistent mechanistic framework for CD24-mediated immunomodulation in severe pneumonia. Although the whole-lung RNA sequencing analysis provided comprehensive insights into immune-related gene expression and the therapeutic mechanism of CD24-ROSμNG, its limited capacity to resolve cell-specific gene profiles underscored the need for complementary single-cell RNA sequencing in future studies.

Therapeutic effect of CD24-ROSμNG on influenza viral pneumonia

Building upon the promising therapeutic efficacy demonstrated in LPS-induced severe acute pneumonia, we further explored the therapeutic potential of CD24-ROSμNG in influenza virus-infected Balb/c mice. The pathogen-driven model that more faithfully recapitulates the clinical scenario by integrating both DAMP-mediated inflammation and antiviral immune responses was established by intranasal instillation of H1N1 virus [10 × median lethal dose (LD_{50})] as illustrated in Fig. 6A. H&E staining and lung injury scores demonstrated that CD24-ROSμNG monotherapy significantly reduced lung injury, with only slight alveolar wall thickening and largely preserved parenchymal architecture (Fig. 6B and fig. S45). The combination therapy of CD24-ROSμNG and zanamivir achieved superior efficacy, demonstrating near-intact lung tissue morphology and a 95% reduction in viral load (Fig. 6C). In contrast, monotherapy with zanamivir at equivalent dosage showed minimal antiviral activity and negligible tissue protection, signifying the indispensable contribution of CD24 nanogels in augmenting the efficacy of antiviral therapeutics for severe infectious pneumonia. ELISA and quantitative polymerase chain reaction (qPCR) analysis revealed that CD24 nanogels reduced proinflammatory cytokines (IL-1β, IL-6, and TNF-α) in the lung tissues (Fig. 6, D to F, and fig. S46). Compared to the PBS group, CD24-ROSμNG and the combination group reduced proinflammatory cytokine levels by more than 40 and 60%, respectively, while zanamivir displayed little anti-inflammatory effect. Besides, CD24-ROSμNG alleviated cytokine storm-mediated tissue damage through immunomodulation coupled with preservation of antiviral immunity, showing a unique therapeutic strategy with antiviral agents in treating severe infectious pneumonia.

The infiltration level of macrophages in lung tissue was significantly suppressed by CD24 nanogels, in which CD24-ROSμNG showed a 35% reduction in macrophage infiltration and the combination therapy group revealed a comparable macrophage level to healthy controls (Fig. 6, G and H). The macrophage reduction may stem from inflammation resolution, as CD24-ROSμNG suppresses proinflammatory cytokines and chemotaxis to limit macrophage recruitment, ultimately leading to the apoptosis or migration of macrophages. In contrast, neutrophil levels displayed a distinct inverse pattern, showing paradoxical neutrophil accumulation alongside a decrease in macrophage infiltration (Fig. 6, I and J, and fig. S47). Compared to PBS and zanamivir controls, CD24-ROSμNG treatment induced twofold increase in neutrophil levels. Neutrophils execute multifaceted antiviral defenses (phagocytosis, degranulation, ROS generation, and NETosis) while balancing their pathogenic potential through neutrophil extracellular trap (NET)–driven cytotoxicity and cytokine storm amplification (*64*–*66*). ELISA assays detected attenuated NETosis biomarkers (H3cit-NE complexes) in treated lungs (Fig. 6K). In vitro assays verified dose-dependent NETosis inhibition of CD24-ROSμNG, with SYTOX $Green^{+}$ extracellular DNA signals (indicative of dysregulated NETosis) showing an 80% reduction compared to R848-stimulated PBS controls (Fig. 6, L and M). Thus, CD24-mediated NETosis inhibition prevented rapid neutrophil death and extended their tissue retention, and these accumulated neutrophils retained antiviral activity. Diminished NET formation also disrupted the NET-DAMP–macrophage inflammatory amplification loop, further restraining macrophage activation. This coordination of decreased macrophages, increased neutrophils, and restricted NET-driven DAMP signaling affords a favorable therapeutic balance, where hyperinflammation and tissue damage are controlled while antiviral defense is preserved.

Viral phagocytosis assays and neutrophil depletion experiments were conducted to evaluate the antiviral function of neutrophils. Normal neutrophils, R848-stimulated neutrophils (NETosis), and CD24-ROSμNG/R848–treated neutrophils were cocultured with green fluorescent protein (GFP)–expressing virus and Madin-Darby canine kidney (MDCK) host cells. Antiviral capability was assessed by monitoring GFP fluorescence intensity, and the results showed that neutrophils demonstrated potent antiviral activity, effectively eliminating viruses within host cells (fig. S48). Notably, CD24 appeared to modulate neutrophil response by maintaining functional integrity while attenuating excessive R848-induced NETosis progression, thereby retaining robust antiviral efficacy. Emerging evidence indicates that CD24 exerts selective immunomodulatory effects by activating Siglec-9/E signaling, a pathway linked to inhibition of NET formation and neutrophil programmed death (*67*, *68*). This dual regulatory capacity suggests Siglec-9/E pathway activation as a plausible mechanism for CD24-mediated NETosis inhibition, potentially preserving or enhancing pulmonary neutrophil-associated antiviral immunity. DCFH-DA fluorescent probe analysis revealed that ROSμNG exhibited minimal impact on ROS levels in normal neutrophils as demonstrated by a slight reduction in fluorescence intensity (fig. S49), suggesting that ROSμNG is unlikely to impair the ability of neutrophils to eliminate pathogens through oxidative mechanisms. Therapeutic evaluation in H1N1 influenza pneumonia models displayed that CD24-ROSμNG demonstrated superior efficacy, with all treated mice maintaining stable body weight and surviving the intervention (Fig. 6, N and O), markedly outperforming Dex (14% survival) and zanamivir (71% survival) treatment groups. These findings propose an innovative therapeutic strategy to address the critical clinical challenge of simultaneously managing hyperinflammation and maintaining essential immune defenses during severe pulmonary infections.

This study demonstrates that inhalable CD24-ROSμNG can rescue acute severe pneumonia through selective inhibition of

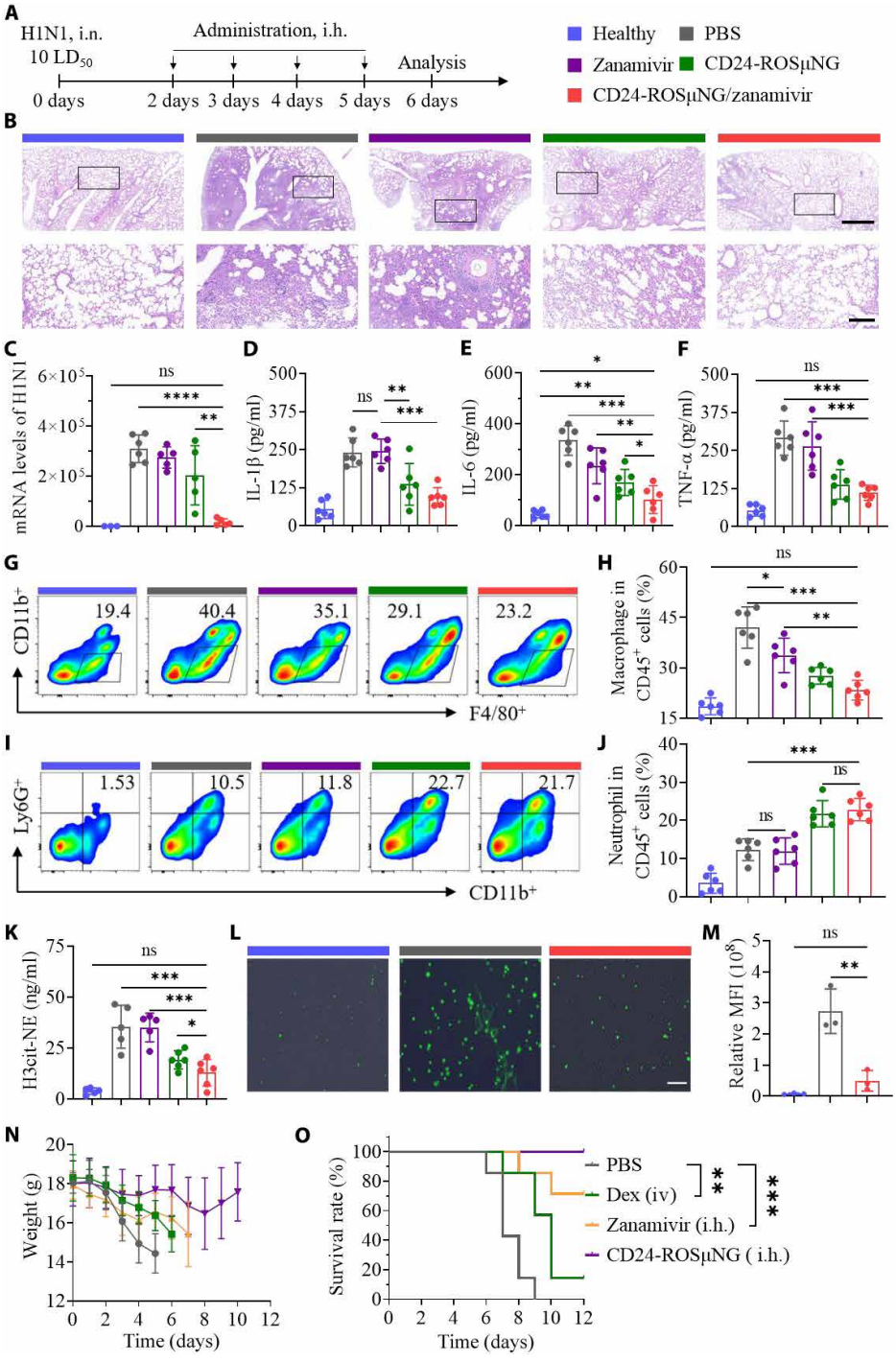

Fig. 6. Treatment of H1N1 viral pneumonia. (**A**) Therapeutic regimen for acute viral pneumonia in Balb/c mice intranasally infected with H1N1 virus (A/PR/8/34 strains, 10 × LD_{50}) ($n = 6$). Two days postinfection, different formulations were administered via nebulization for four consecutive days. (**B**) Representative H&E staining of lung tissue. Bottom panels show magnified images at the locations indicated in the top panels. Scale bars, 1 mm and 200 μm for overview and magnified images, respectively. (**C**) Viral mRNA expression in the lung tissues measured by PCR ($n = 6$). Levels of IL-1β (**D**), IL-6 (**E**), and TNF-α (**F**) in the lung tissues ($n = 6$). Representative flow cytometry analysis images of $CD11b^{+lo}$ $F4/80^{+hi}$ cells in the total CD45 cell population (**G**) and quantitative analysis of cell proportions (**H**) ($n = 6$). Representative flow cytometry analysis images of $CD11b^{+}$ $Ly6G^{+}$ cells in the total CD45 cell population (**I**) and quantitative analysis of cell proportions (**J**) ($n = 6$). (**K**) Levels of H3cit-NE in the lung tissues ($n = 6$). (**L**) Representative images of NET levels after treatment with CD24-ROSμNG in neutrophils ($n = 3$). The DNA in NET was visualized by staining with SYTOX Green (green). (**M**) Semiquantitative of NET levels (SYTOX Green fluorescence intensity) in neutrophils analyzed by ImageJ ($n = 3$). (**N**) The weight change and (**O**) survival rate of Balb/c mice infected with H1N1 influenza virus (A/PR/8/34 strains, 10 × LD_{50}, $n = 7$). Two days postinduction, the mice were administered once daily for consecutive 4 days with PBS, Dex (1.5 mg/kg, iv), zanamivir [5.0 mg/kg, inhalation (i.h.)], or CD24-ROSμNG (CD24: 1.5 mg/kg, i.h.). *$P < 0.05$; **$P < 0.01$; ***$P < 0.001$; ****$P < 0.0001$; ns, not significantly different at $P > 0.05$.

hyperinflammatory response. CD24-ROSμNG exhibits high stability against nebulization, enhanced mucosal penetration, and targeted drug release profiles. In murine models of severe acute pneumonia, inhaled CD24-ROSμNG achieves rapid pulmonary enrichment and effectively modulates immune response, affording suppression of inflammatory cascades, mitigation of oxidative stress, attenuation of lung injury, and marked improvement of survival outcomes. In H1N1-induced pneumonia models, CD24-ROSμNG displays selective control of pathogenic inflammation coupled with preservation and augmentation of neutrophil-mediated antiviral immunity. This balanced immunomodulation enables effective pathogen clearance while preventing infection-associated immunopathology, holding broad applicability in pathogen-driven severe pneumonia. Furthermore, the markedly enhanced efficacy observed with low-dose antiviral coadministration highlights the potential as a complementary therapeutic strategy of CD24-ROSμNG in clinical practice. Thus, the inhalable CD24 nanotherapeutics hold substantial translational potential to augment current regimens for managing critical pulmonary diseases.

MATERIALS AND METHODS

Preparation of HA derivatives and functionalized PEG

HA-DBCO and HA-N_3 were synthesized by amidation reaction. Taking HA-DBCO as an example, HA (100 mg, 264 μmol of —COOH) and DBCO-NH_2 (21.85 mg, 79.2 μmol) were dissolved in a mixture of deionized (DI) water and dimethyl sulfoxide (DMSO; v:v = 1:2, 20 ml), followed by the addition of 4-(4,6-dimethoxy-1,3,5-triazin-2-yl)-4-methylmorpholinium chloride (DMTMM) (32.8 mg, 118.8 μmol). The reaction was conducted at 37°C for 48 hours. Subsequently, the raw product was dialyzed [molecular weight cut-off (MWCO): 3500 Da] with a mixture of DMSO and water (v:v = 1:1). After being dialyzed with DI water to remove DMSO, the product was freeze-dried, with a yield of 92.0%. For the synthesis of HA-N_3, HA (100 mg, 264 μmol —COOH) and triazido propylamine (26.42 mg, 264 μmol) were added in a mixture of DI water and DMSO (v:v = 1:2, 20 ml), followed by the addition of DMTMM (115 mg, 264 μmol). The reaction was conducted at 37°C for 48 hours, yielding 85.3%. The DS of HA-DBCO was 12.5, calculated according to the integral area ratio of the methyl proton signal (—CH_3, δ = 1.5 to 1.9) to the benzene ring proton signal (—C_6H_4, δ = 7.0 to 7.6) in the ^{1}H NMR spectrum. DS of HA-N_3 was 17.5, calculated according to the integral area ratio of the methyl proton signal (—CH_3, δ = 2.0) to the methylene proton signal of 3-azido-1-propanamine (N_3—CH_2—CH_2—CH_2—NH, δ = 1.75) in the ^{1}H NMR spectrum. The molecular weight and molecular weight distribution of the polymers were analyzed by GPC. An aqueous mobile phase containing $NaNO_3$ and NaH_2PO_4 (adjusted to pH 9 with NaOH) was used. A calibration curve was established using PEG standards.

4arm PEG-TK-N_3 was synthesized by two-step amidation of 4arm PEG-NH_2 with bis(carboxy)thioketone and 3-azidopropylamine. Briefly, 4arm PEG-NH_2 (400 mg, 0.32 mmol —NH_2) and bis(carboxy) thioketone (800 mg, 3.20 mmol) were dissolved in MeOH (15 ml), followed by the addition of DMTMM (883 mg, 3.20 mmol). The reaction was conducted at 37°C for 48 hours. Subsequently, the solution was dialyzed with MeOH for 48 hours (MWCO: 3500 Da), and the solvent was evaporated to obtain 4arm PEG-TK-COOH. To obtain 4arm PEG-TK-N_3, 4arm PEG-TK-COOH (250 mg, 0.048 mmol), triazido propylamine (57.6 mg, 0.576 mmol), and DMTMM (26.5 mg, 0.096 mmol) were dissolved in MeOH (10 ml). The reaction was conducted at 37°C for 48 hours. The raw product was dialyzed with MeOH for 48 hours (MWCO: 3500), and the solvent was evaporated to obtain 4arm PEG-TK-N_3. The structure was characterized by ^{1}H NMR, and the DS of N_3 was determined by comparing the integral area of the methyl protons of TK (—CH_3, δ = 1.6), the methylene protons of triazido propylamine (—CH_2, δ = 1.8, 3.38), and the methylene protons of PEG (—CH_2, δ = 3.6) and resulted to 3.9.

ROSμNG preparation and protein encapsulation

ROSμNG was prepared from HA-DBCO and 4arm PEG-TK-N_3 by combining click reaction and nanoprecipitation (*69*). Briefly, HA-DBCO and 4arm PEG-TK-N_3 were mixed in phosphate buffer (PB; pH 7.4, 10 mM) at a DBCO/N_3 molar ratio of 1:1 to obtain a final polymer concentration of 10 mg/ml. The polymer solution (200 μl) was injected into 20 ml of acetone via a syringe, and the mixture was stirred at 25°C for 30 min to form nanogels. After removing the solvent via evaporation, the crude product was dialyzed with PB (MWCO: 3500 Da) to obtain ROSμNG. By replacing 4arm PEG-TK-N_3 with either 4arm PEG-N_3 or HA-N_3, μNG and NG controls were prepared accordingly. The cross-linking efficiency was monitored by UV-Vis and FTIR spectroscopy.

For protein-loaded nanogels, HA derivatives and proteins were premixed at specified feed ratios before injection into acetone. Protein quantification was performed via UV spectrophotometry at 205/280 nm. The PLC and protein encapsulation efficiency (PLE) were calculated according to the following equations

$$\text{PLC (wt\%)} = \left(\text{weight of loaded protein} / \text{weight of loaded protein and nanogels} \times 100\right)$$

$$\text{PLE (\%)} = \left(\text{weight of loaded protein} / \text{weight of fed protein}\right) \times 100$$

The nanogel morphology was observed using transmission electron microscopy (TEM) at an accelerating voltage of 120 kV. The sizes and PDI of nanogels were characterized by dynamic light scattering (DLS). Colloidal stability of nanogels was determined by monitoring the size change following nebulization at 25°C, storage at 4°C for 28 days, and incubation in Dulbecco's modified Eagle's medium containing 10% (v/v) FBS at 37°C for 4 hours. Protein stability against nebulization and trypsin degradation was investigated using CD24 ELISA Kit (JINGMEI Biotechnology). The nanogel suspensions (CD24: 500 μg/ml) were aerosolized via a MicroSprayer aerosolizer (model YAN30012, Shanghai Yuyan Scientific Instrument Co., Ltd.), generating inhalable droplets with an average diameter of less than 30 μm. For intratracheal delivery, anesthetized mice were administered the aerosol through precise positioning of the spray tip near the bronchial bifurcation following oral cavity insertion. The administered volume was precisely controlled at 50 μl per dose. Then, the nebulized samples were collected, and after dialysis against PBS (MWCO: 350 kDa), the protein concentration was quantified by UV absorbance measurement, and the activity of the released protein was subsequently assessed using an ELISA kit. Proteolytic resistance analysis was used to evaluate the stability of CD24 loaded in nanogels. The nanogels (CD24: 500 μg/ml) were treated with trypsin (2.5 mg/ml) for 4 hours, and the residual bioactivity of CD24 was similarly determined through the ELISA kit after dialysis against DI water to remove trypsin.

In vitro mucus penetration of nanogels

Artificial airway mucus was prepared according to a previously described protocol (*36*, *70*). Mucin solution (43.75 mg/ml), calcium carbonate suspension (14.0 mg/ml), D-gluconate-δ-lactone (49.84 mg/ml), and sodium alginate (21.0 mg/ml) prepared 1 day in advance were mixed at a volume ratio of 4:1:1:1 under magnetic stirring for 3 hours to ensure homogeneous mixing. For mucus permeation analysis, the synthesized artificial mucus was loaded into both the lower and the upper chambers of a 24-well transwell plate. Then, the nanogels loaded with CD24-Cy5 were added to the upper chamber, followed by incubation on a shaker (200 rpm) at 37°C for 4 hours. After removing the upper chamber, the fluorescence intensity in the lower chamber was measured using In Vivo Imaging System (IVIS) to calculate mucus permeation efficiency. The morphological changes of CD24-ROSμNG in artificial mucus were observed using cryo-SEM (Polaris Research Services).

The nanomechanical properties of the nanogels and artificial lung mucus were further characterized under liquid conditions using PeakForce Quantitative Nanomechanical Mapping (PeakForce QNM) mode on a Dimension XR atomic force microscope (Bruker). An SNL-10 cantilever probe (Bruker) with a nominal spring constant of 0.12 N/m, a tip radius of ~20 nm, and a resonant frequency of around 23 kHz was used. Measurements were conducted in PBS solution at a scanning rate of 0.9 Hz, and the pressing depth is less than 10% of the sample thickness. In force spectroscopy mode, force-distance curves were recorded at multiple random locations using a closed-loop Z-piezo control system, with 10 to 15 curves collected and averaged per sample to obtain representative mechanical parameters.

ROS-responsive protein release

For protein release profiling, Cy5-labeled CD24 was encapsulated into the nanogels. Release kinetics were monitored by immersing CD24-loaded formulations (100 μl) in PBS containing gradient H_2O_2 (0, 0.1, 1.0, and 10 mM) or HAase (0, 10, and 20 U/ml) under sink conditions (1:20 volume ratio, 200 rpm, 37°C). At predetermined time points, the supernatant was replaced for fluorescence quantification using a multimode microplate reader. The secondary structure of released CD24 (300 μg/ml) from nebulized CD24-ROSμNG was analyzed by CD spectroscopy (J-815, JASCO) at a wavelength of 190 to 250 nm.

ROS-responsive degradation of ROSμNG was investigated by monitoring particle size changes via DLS following the treatment with 1.0 and 10 mM H_2O_2 for 12 hours. The triggered cleavage of 4arm PEG-TK-N_3 was investigated in the presence of H_2O_2. Briefly, 4arm PEG-TK-N_3 (5.0 mg) was treated with H_2O_2 at different concentrations (1, 10, and 100 mM) for 6 hours at 37°C under shaking (200 rpm). After lyophilization, the resulting products were dissolved in CD_3OD for ^1H NMR analysis.

ROS scavenging efficacy of nanogels was evaluated in the presence of H_2O_2. Specifically, 1.0 ml of nanogel suspensions (ROSμNG: 0.5, 1.0, and 2.0 mg/ml; μNG: 0.5 mg) placed in dialysis bags (MWCO: 3500 Da) was soaked in 1.0 ml of H_2O_2 (50, 100 150, and 200 μM). After incubation at 37°C with shaking (200 rpm) for 1 hour, residual H_2O_2 levels were measured using an H_2O_2 assay kit, and scavenging efficiency was calculated relative to untreated controls.

Cytocompatibility and cellular uptake

The cytocompatibility of nanogels was evaluated using CCK-8 assay. RAW264.7 cells were seeded at a density of 1×10^4 per well in 96-well plates for 12 hours. Then, CD24-ROSμNG solutions with different CD24 concentration (0 to 100 μg/ml) were added. After a 48-hour treatment, cell viability was assessed using the CCK-8 assay kit.

Cellular uptake of nanogels was evaluated using flow cytometry and confocal laser scanning microscopy (CLSM). For CLSM imaging, RAW264.7 cells were seeded in 35-mm confocal dishes at a density of 2×10^5 cells per dish for 12 hours. Following stimulation with LPS (1.0 μg/ml) for 2 hours, the cells were treated with nanogels loaded with CD24-Cy5 (CD24: 10 μg/ml) for 4 hours. After washing with PBS, the nuclei were stained with 4′,6-diamidino-2-phenylindole (DAPI) for CLSM imaging. For flow cytometry assay, RAW264.7 cells were seeded in 24-well plates at 1×10^5 cells per well and treated with LPS and nanogels under similar conditions. Cellular fluorescence intensity and $Cy5^+$ cell populations were quantified via flow cytometry at 1, 2, and 4 hours posttreatment.

In vitro anti-inflammatory effects of CD24-ROSμNG

Cytokine profiling was performed to evaluate in vitro anti-inflammatory effects. RAW264.7 cells were seeded in 24-well plates at a density of 1×10^5 cells per well overnight. Following the stimulation with LPS (1.0 μg/ml) and HMGB-1 (5.0 μg/ml) for 2 hours, the cells were treated with PBS, ROSμNG (0.5 and 5.0 μg/ml), free CD24, CD24-ROSμNG, CD24-μNG, or CD24-NG for 24 hours. CD24 concentration was fixed at 150 ng/ml, and the levels of IL-6 and IL-10 in the supernatants were measured using ELISA kits.

To investigate DAMP-dependent inflammatory modulation, LPS-stimulated cells were treated with HMGB-1 (0 to 5.0 μg/ml) and CD24-ROSμNG (CD24: 300 ng/ml) for 24 hours. IL-6 levels were measured by ELISA, with unstimulated cells as controls. To examine the mechanism of CD24 in inflammation control, RAW264.7 cells were pretreated with NSC-87877 for 2 hours, stimulated with HMGB-1 (5.0 μg/ml) or LPS (1.0 μg/ml) + HMGB-1 (5.0 μg/ml) for 2 hours, and then treated with CD24-ROSμNG (CD24: 300 ng/ml) for 24 hours. IL-6 levels were quantified via ELISA.

Intracellular ROS levels as a critical factor of inflammation was measured using DCFH-DA assay. RAW264.7 cells were pretreated with LPS (1.0 μg/ml) and HMGB-1 (5.0 μg/ml) for 2 hours and then incubated with different formulations (CD24: 150 ng/ml) for 24 hours. After washing with PBS, the cells were incubated with DCFH-DA (10 μM) for 30 min, and the fluorescence was visualized by an inverted microscope and the intensities were quantified with ImageJ to determine intracellular ROS levels.

Western blot analysis was used to investigate the anti-inflammatory mechanism of CD24 at the cellular level. RAW264.7 cells were treated with LPS (1 μg/ml) for 2 hours, followed by a 24-hour treatment with PBS, CD24-ROSμNG (CD24: 150 ng/ml), or CD24-ROSμNG (CD24: 150 ng/ml) combined with NSC-87877 (10 μM). After treatment, cells were collected, washed twice with PBS, and fully lysed using moderate radioimmunoprecipitation assay (RIPA) lysis buffer supplemented with phosphatase and protease inhibitors to extract total protein. The primary antibodies used included IκB Alpha Proteintech Rabbit Polyclonal Antibody, Phospho-NF-κB p65 (Ser^{468}) Recombinant Antibody, and NF-κB p65 Recombinant Antibody (Fcmacs Biotech Co., Ltd.). A glyceraldehyde-3-phosphate dehydrogenase antibody served as the internal loading control.

In vitro NETosis inhibition was investigated using SYTOX Green kit. Isolated neutrophils in 48-well plates (5×10^4 cells per well) were treated with PBS, R848 (10 μg/ml), or R848 + CD24-ROSμNG (CD24: 300 ng/ml) for 8 hours. SYTOX Green staining

was performed, and the cells were observed under an inverted fluorescence microscope.

In the validation experiment investigating the effect of CD24 on the antiviral capacity of neutrophils in vitro, experiments were conducted using genetically stable GFP-labeled H1N1 virus. First, neutrophils were isolated from mouse bone marrow and divided into three groups: untreated cells, cells treated with R848 (10 μg/ml), and cells cotreated with R848 (10 μg/ml) and CD24-ROSμNG (CD24: 300 ng/ml) for 2 hours. MDCK cells were seeded in a 12-well plate at a density of 1×10^5 cells per well. After 24 hours, when the cell confluency reached ~60%, the treated neutrophils (5×10^4 cells) and H1N1 virus (at a multiplicity of infection of 0.001) were simultaneously added to the MDCK cell cultures. At 24 and 36 hours postinfection, GFP signals were observed using an inverted fluorescence microscope (Ex: 479 nm; Em: 520 nm). The fluorescence was visualized by an inverted microscope, and the intensities were quantified with ImageJ to determine intracellular ROS levels.

In vivo biodistribution of CD24-ROSμNG

An acute pneumonia model was established in Balb/c mice through inhalation (i.h.) administration of LPS (*38*). Two hours postinduction, the mice were treated via intratracheal nebulization with CD24-ROSμNG, CD24-μNG, or CD24-NG (CD24: 1.5 mg/kg). At predetermined time points (0, 3, 6, 12, and 24 hours), mice were euthanized, and major organs were collected for ex vivo imaging using an IVIS system. BALF and serum were collected from mice in each group at designated time points (3, 6, and 24 hours). The concentration of free protein in these samples was then measured using an ELISA kit. The sample processing shall be carried out in accordance with the requirements of the instruction manual.

In vivo therapeutic efficacy in severe pneumonia

A murine model of severe acute pneumonia was established in Balb/c mice via intratracheal instillation of LPS (*18*). Considering the clinical dose of CD24 (480 mg per patient) for pneumonia treatment (*17*) and the low pulmonary bioavailability of intravenously administered protein therapeutics (*71*, *72*), mice were administered once daily for three consecutive days via nebulization with CD24-ROSμNG (CD24: 0.25, 0.75, and 1.5 mg/kg) 2 hours postinduction by LPS. CD24-μNG (CD24: 1.5 mg/kg), ROSμNG (6.0 mg/kg) + free CD24 (1.5 mg/kg), ROSμNG (6.0 mg/kg), and PBS served as controls. Two hours postinduction, the mice were administered once daily for three consecutive days via nebulization with PBS, ROSμNG (6.0 mg/kg), ROSμNG (6.0 mg/kg) + free CD24 (1.5 mg/kg), CD24-μNG (CD24: 1.5 mg/kg), or CD24-ROSμNG (CD24: 0.25, 0.75, and 1.5 mg/kg). Healthy mice served as controls. At 24 hours after the last dose, euthanasia was performed for tissue collection. One lung lobe was immediately weighed to determine wet weight and then desiccated in an oven at 65°C for 72 hours to obtain dry weight. The lung W/D weight ratios were used to assess the pulmonary edema levels. For histopathological evaluation, the lung tissues were fixed in 4% paraformaldehyde (PFA), sectioned, and stained with H&E, Tunel, DAPI, and MPO. The lung injury was assessed using a four-tier grading system based on inflammatory infiltration, necrosis, wall thickness, edema, and hemorrhage. Meanwhile, lung tissues were homogenized in RIPA buffer, and the supernatants were collected for the analysis of MDA, LDH, and cytokines (IL-1β, IL-6, IL-10, TNF-α, and IFN-γ) using commercial kits. Serum IL-6 and IL-10 were concurrently measured. To assess the macrophage infiltration, cells in the lung tissues were isolated and stained with fluorescent antibodies against CD45, CD11b, and F4/80 for flow cytometry analysis.

For RNA sequencing, lung tissues from healthy, LPS-treated, and CD24-ROSμNG–treated mice ($n = 3$ per group) were snap-frozen and processed by Novogene. Raw data underwent quality control (sequencing error rates, base distribution, and filtering) on the Novomagic Cloud Platform. Clean reads were aligned to the reference genome using HISAT2, followed by gene expression quantification via featureCounts (Subread package), excluding low-quality (mapping quality score < 10), improperly paired, or multiple-mapped reads. PCA on Fragments Per Kilobase of transcript per Million mapped reads (FPKM) values assessed sample variability and reproducibility. Differential expression analysis involved DESeq2 normalization, negative binomial model for *P* value, and Benjamini-Hochberg False Discovery Rate (FDR) correction (BH-FDR; *P* adj). DEGs were defined as those with a *P* adj (BH-FDR) < 0.05 and an absolute $\log_2$ fold change (FC) ≥ 1. Functional enrichment GO/KEGG was performed using cluster profiler via hypergeometric testing, comparing DEG test set against all genes background.

A fatal acute pneumonia model was built via intratracheal instillation of LPS (50 mg/kg) in Balb/c mice for the survival assessment (*38*). Two hours postinduction, the mice were treated with PBS, ROSμNG (6.0 mg/kg), CD24-NG (CD24: 1.5 mg/kg), CD24-μNG (CD24: 1.5 mg/kg), or CD24-ROSμNG (CD24: 1.5 mg/kg) (i.h.) once daily for three consecutive days. Intravenous injection of free CD24 (55.0 mg/kg, single dose) and Dex (1.5 mg/kg, once daily for three consecutive days) was used as control. Survival was monitored for 7 days. Lung tissues were harvested from CD24-ROSμNG–treated mice 1 week and 1 month after the completion of the therapeutic monitoring period and subsequently subjected to histological analysis via H&E and Masson's trichrome staining.

Healthy Balb/c mice were administered with CD24-ROSμNG (CD24: 15.0 mg/kg) via nebulization to evaluate the in vivo safety. Major organs including the hearts, livers, spleens, and kidneys were collected at 24 hours for H&E-stained histological analysis. Serum was collected after anesthetization on days 7, 14, and 28 posttreatment for subsequent assessment of liver/kidney function and hematological parameters.

In vivo therapeutic efficacy in viral pneumonia

A viral pneumonia model was generated via intranasal inoculation with $10 \times LD_{50}$ of H1N1 influenza virus. Two days postinfection, mice were treated once daily for four consecutive days via nebulization with PBS, zanamivir (3.0 mg/kg), CD24-ROSμNG (CD24: 1.5 mg/kg), or combination therapy to comprehensively evaluate the therapeutic effect of CD24-ROSμNG in viral pneumonia. Zanamivir at a dose of 3.0 mg/kg (once daily for 4 days) was selected based on prior studies (*73*–*75*). At 24 hours after the last treatment, mice were euthanized by cervical dislocation, and the lung tissues were collected for histopathological evaluation and inflammatory analysis as described above. To assess the macrophage and neutrophil infiltration, cells in the lung tissues were isolated and stained with fluorescent antibodies against CD45, CD11b, F4/80, and Ly6G for flow cytometry analysis. Besides, the virus loading levels and cytokine gene expression in lung tissues were analyzed by qPCR. RNA was extracted from lung tissues (5.0 mg) using a commercial RNA extraction kit, and a comprehensive list of all primers used was provided in table S2. To analyze the levels of NETs, the lung tissues were processed according to the

specification, and the level of the NET marker H3cit-NE was detected using an ELISA kit.

The therapeutic efficacy of CD24-ROSμNG was evaluated in the aforementioned murine model of H1N1 viral pneumonia. The dose of zanamivir (5.0 mg/kg, once daily for 4 days) was derived from the clinical therapeutic dose (*76*). Two days postinduction, the mice were administered once daily for four consecutive days with PBS, Dex (1.5 mg/kg, iv), zanamivir (5 mg/kg, i.h.), or CD24-ROSμNG (CD24: 1.5 mg/kg, i.h.). Survival was monitored for 12 days.

Ethics statement

Pathogen-free male Balb/c mice (6 to 8 weeks old) were purchased from Charles River Laboratories (Shanghai, China). Animal experiments including the model establishment, treatment, and characterization of severe and lethal pneumonia were approved by the Animal Care and Use Committee of Soochow University (approval no. SUDA20250508A027). The establishment, treatment, and characterization of mouse viral infectious pneumonia were approved by Institutional Animal Care and Use Committee of the Institute of Systems Medicine, Suzhou (approval no. ISM-IACUC-20250115).

Supplementary Materials

This PDF file includes:

Supplementary Text
Tables S1 and S2
Figs. S1 to S50
References

REFERENCES

1. A. Torres, C. Cilloniz, M. S. Niederman, R. Menéndez, J. D. Chalmers, R. G. Wunderink, T. van der Poll, Pneumonia. *Nat. Rev. Dis. Primers* **7**, 25 (2021).
2. V. M. Vaughn, R. P. Dickson, J. K. Horowitz, S. A. Flanders, Community-acquired pneumonia: A review. *JAMA* **332**, 1282–1295 (2024).
3. K. Xie, S. Guan, X. Kong, W. Ji, C. Du, M. Jia, H. Wang, Predictors of mortality in severe pneumonia patients: A systematic review and meta-analysis. *Syst. Rev.* **13**, 210 (2024).
4. S. Aliberti, C. S. Dela Cruz, F. Amati, G. Sotgiu, M. I. Restrepo, Community-acquired pneumonia. *Lancet* **398**, 906–919 (2021).
5. L. Hiti, T. Markovic, M. Lainscak, J. Farkas Lainscak, E. Pal, I. Mlinaric-Rascan, The immunopathogenesis of a cytokine storm: The key mechanisms underlying severe COVID-19. *Cytokine Growth Factor Rev.* **82**, 1–17 (2025).
6. K. E. Traber, J. P. Mizgerd, The integrated pulmonary immune response to pneumonia. *Annu. Rev. Immunol.* **43**, 545–569 (2025).
7. H. Ledford, Coronavirus breakthrough: Dexamethasone is first drug shown to save lives. *Nature* **582**, 469 (2020).
8. A. I. Ritchie, A. Singanayagam, Immunosuppression for hyperinflammation in COVID-19: A double-edged sword? *Lancet* **395**, 1111 (2020).
9. E. Pontali, S. Volpi, A. Signori, G. Antonucci, M. Castellaneta, D. Buzzi, A. Montale, M. Bustaffa, A. Angelelli, R. Caorsi, E. Giambruno, N. Bobbio, M. Feasi, I. Gueli, F. Tricerri, F. Calautti, E. Castagnola, A. Moscatelli, G. A. Rollandi, A. Ravelli, G. Cassola, M. P. Sormani, M. Gattorno, Efficacy of early anti-inflammatory treatment with high doses of intravenous anakinra with or without glucocorticoids in patients with severe COVID-19 pneumonia. *J. Allergy Clin. Immunol.* **147**, 1217–1225 (2021).
10. S. Zhang, L. Li, A. Shen, Y. Chen, Z. Qi, Rational use of tocilizumab in the treatment of novel coronavirus pneumonia. *Clin. Drug Investig.* **40**, 511–518 (2020).
11. G. Chen, N. Li, X. Dai, S. Tu, Z. Shen, K. Wu, T. Jin, J. Wu, C. Peng, G. Sheng, M. Zhu, L. Tang, L. Li, Safety, tolerability, pharmacokinetics, and pharmacodynamics of anti-C5a antibody BDB-001 for severe COVID-19: A randomized, double-blind, placebo-controlled phase 1 clinical trial in healthy Chinese adults. *Infect. Dis. Ther.* **12**, 663–675 (2023).
12. G. W. Strohbehn, B. L. Heiss, S. J. Rouhani, J. A. Trujillo, J. Yu, A. J. Kacew, E. F. Higgs, J. C. Bloodworth, A. Cabanov, R. C. Wright, A. K. Koziol, A. Weiss, K. Danahey, T. G. Karrison, C. C. Edens, I. Bauer Ventura, N. N. Pettit, B. K. Patel, J. Pisano, M. E. Strek, T. F. Gajewski, M. J. Ratain, P. D. Reid, COVIDOSE: A phase II clinical trial of low-dose tocilizumab in the treatment of noncritical COVID-19 pneumonia. *Clin. Pharmacol. Ther.* **109**, 688–696 (2021).
13. S. Wang, Y. Zhang, HMGB1 in inflammation and cancer. *J. Hematol. Oncol.* **13**, 116 (2020).
14. M. Deng, Y. Tang, W. Li, X. Wang, R. Zhang, X. Zhang, X. Zhao, J. Liu, C. Tang, Z. Liu, Y. Huang, H. Peng, L. Xiao, D. Tang, M. J. Scott, Q. Wang, J. Liu, X. Xiao, S. Watkins, J. Li, H. Yang, H. Wang, F. Chen, K. J. Tracey, T. R. Billiar, B. Lu, The endotoxin delivery protein HMGB1 mediates caspase-11-dependent lethality in sepsis. *Immunity* **49**, 740–753 (2018).
15. G.-Y. Chen, J. Tang, P. Zheng, Y. Liu, CD24 and Siglec-10 selectively repress tissue damage-induced immune responses. *Science* **323**, 1722–1725 (2009).
16. X. Fang, P. Zheng, J. Tang, Y. Liu, CD24: From A to Z. *Cell. Mol. Immunol.* **7**, 100–103 (2010).
17. C. M. Eckhardt, M. R. O'Donnell, CD24Fc: An emerging COVID-19 therapy. *Lancet Infect. Dis.* **22**, 565–567 (2022).
18. S. Shapira, M. Ben Shimon, M. Hay-Levi, G. Shenberg, G. Choshen, L. Bannon, M. Tepper, D. Kazanov, J. Seni, S. Lev-Ari, M. Peer, D. Boubas, J. Stebbing, S. Tsiodras, N. Arber, A novel platform for attenuating immune hyperactivity using EXO-CD24 in COVID-19 and beyond. *EMBO Mol. Med.* **14**, e15997 (2022).
19. Z. Jin, Q. Gao, K. Wu, J. Ouyang, W. Guo, X.-J. Liang, Harnessing inhaled nanoparticles to overcome the pulmonary barrier for respiratory disease therapy. *Adv. Drug Deliv. Rev.* **202**, 115111 (2023).
20. Y. Wang, R. Y. K. Chang, W. J. Britton, H.-K. Chan, Advances in the development of antimicrobial peptides and proteins for inhaled therapy. *Adv. Drug Deliv. Rev.* **180**, 114066 (2022).
21. E. S. Fung, J. A. Parker, A. M. Powell, A. Maier, Estimating inhalation bioavailability for peptides and proteins 1 to 10 kDa in size. *Regul. Toxicol. Pharmacol.* **137**, 105314 (2023).
22. L. Yue, X. Zhang, C. Zhao, R. Chen, X. Chen, L. Rao, Inhaled drug delivery: Past, present, and future. *Nano Today* **52**, 101942 (2023).
23. F. Tan, X. Li, Z. Wang, J. Li, K. Shahzad, J. Zheng, Clinical applications of stem cell-derived exosomes. *Signal Transduct. Target. Ther.* **9**, 17 (2024).
24. Y. Yang, F. Tian, D. Nie, Y. Liu, K. Qian, M. Yu, A. Wang, Y. Zhang, X. Shi, Y. Gan, Rapid transport of germ-mimetic nanoparticles with dual conformational polyethylene glycol chains in biological tissues. *Sci. Adv.* **6**, eaay9937 (2020).
25. J. T. Huckaby, S. K. Lai, PEGylation for enhancing nanoparticle diffusion in mucus. *Adv. Drug Deliv. Rev.* **124**, 125–139 (2018).
26. Q. Zhang, Q. Yu, Z. Wu, Z. Chen, Y. Liu, Q. Chen, Y. Yang, Inhalable and transformable nanocapsules with effective mucus-penetrating ability for pulmonary inflammation treatment. *Cell Biomater.* **1**, 100150 (2025).
27. M. Tollemeto, I. Badillo-Ramírez, L. H. E. Thamdrup, Y. Li, M. Ghavami, T. P. Padial, J. B. Christensen, J. van Hest, A. Boisen, A systematic study on the physicochemical interactions between polymeric micelles and mucin: Toward the development of optimal drug delivery nanocarriers. *Adv. Mater. Interfaces* **11**, 2400107 (2024).
28. M. Cherri, P. S. Stergiou, Z. Ahmadian, T. L. Povolotsky, B. Thongrom, X. Fan, E. Mohammadifar, R. Haag, Redox-responsive hydrogels loaded with an antibacterial peptide as controlled drug delivery for healing infectious wounds. *Adv. Healthc. Mater.* **13**, 2401289 (2024).
29. W. Yang, Z. Chen, Y. Qu, P. Ye, Y. Tang, Q. Yu, Z. Zhang, Q. Dai, C. Dou, F. Luo, Pollen-inspired aptamer delivery system for multi-target therapy in rheumatoid arthritis. *Adv. Funct. Mater.* **35**, 2425323 (2025).
30. Q. Zhang, W. Chen, G. Li, Z. Ma, M. Zhu, Q. Gao, K. Xu, X. Liu, W. Lu, W. Zhang, Y. Wu, Z. Shi, J. Su, A factor-free hydrogel with ROS scavenging and responsive degradation for enhanced diabetic bone healing. *Small* **20**, e2306389 (2024).
31. C. A. Bradley, CD24—A novel 'don't eat me' signal. *Nat. Rev. Cancer* **19**, 541 (2019).
32. A. A. Barkal, R. E. Brewer, M. Markovic, M. Kowarsky, S. A. Barkal, B. W. Zaro, V. Krishnan, J. Hatakeyama, O. Dorigo, L. J. Barkal, I. L. Weissman, CD24 signalling through macrophage Siglec-10 is a target for cancer immunotherapy. *Nature* **572**, 392–396 (2019).
33. N.-J. Song, C. Allen, A. E. Vilgelm, B. P. Riesenberg, K. P. Weller, K. Reynolds, K. B. Chakravarthy, A. Kumar, A. Khatiwada, Z. Sun, A. Ma, Y. Chang, M. Yusuf, A. Li, C. Zeng, J. P. Evans, D. Bucci, M. Gunasena, M. Xu, N. P. M. Liyanage, C. Bolyard, M. Velegraki, S.-L. Liu, Q. Ma, M. Devenport, Y. Liu, P. Zheng, C. D. Malvestutto, D. Chung, Z. Li, Treatment with soluble CD24 attenuates COVID-19-associated systemic immunopathology. *J. Hematol. Oncol.* **15**, 5 (2022).
34. S. Xie, N. Fatemipayam, J. Zhang, C. P. Aichele, J. D. Ramsey, Inhalable micro/nanoparticles for pulmonary delivery of macromolecular therapeutics: A review. *Biomaterials* **325**, 123550 (2026).
35. H. Wang, Y. Yuan, L. Qin, M. Yue, J. Xue, Z. Cui, X. Zhan, J. Gai, X. Zhang, J. Guan, S. Mao, Tunable rigidity of PLGA shell-lipid core nanoparticles for enhanced pulmonary siRNA delivery in 2D and 3D lung cancer cell models. *J. Control. Release* **366**, 746–760 (2024).
36. S. Gou, G. Wang, Y. Zou, W. Geng, T. He, Z. Qin, L. Che, Q. Feng, K. Cai, Non-pore dependent and MMP-9 responsive gelatin/silk fibroin composite microparticles as universal delivery platform for inhaled treatment of lung cancer. *Adv. Mater.* **35**, 2303718 (2023).
37. W. Peng, W. Tai, B. Li, H. Wang, T. Wang, S. Guo, X. Zhang, P. Dong, C. Tian, S. Feng, L. Yang, G. Cheng, B. Zheng, Inhalable nanocatalytic therapeutics for viral pneumonia. *Nat. Mater.* **24**, 637–648 (2025).

38. Z. Zhai, W. Ouyang, Y. Yao, Y. Zhang, H. Zhang, F. Xu, C. Gao, Dexamethasone-loaded ROS-responsive poly(thioketal) nanoparticles suppress inflammation and oxidative stress of acute lung injury. *Bioact. Mater.* **14**, 430–442 (2022).
39. J. Guo, J. Huang, Z. Huang, D. Hu, H. Tan, Y. Wang, C. Deng, X. Zhu, Z. Zhong, Tumor vessel-adaptable adhesive and absorbable microspheres for sustainable transarterial chemoembolization therapy. *Nat. Commun.* **16**, 6239 (2025).
40. J. L. Schultze, A. C. Aschenbrenner, COVID-19 and the human innate immune system. *Cell* **184**, 1671–1692 (2021).
41. K. Xiao, Y. Cao, Z. Han, Y. Zhang, L. D. W. Luu, L. Chen, P. Yan, W. Chen, J. Wang, Y. Liang, X. Shi, X. Wang, F. Wang, Y. Hu, Z. Wen, Y. Chen, Y. Yang, H. Yu, L. Xie, Y. Wang, A pan-immune panorama of bacterial pneumonia revealed by a large-scale single-cell transcriptome atlas. *Signal Transduct. Target. Ther.* **10**, 5 (2025).
42. M. Merad, J. C. Martin, Pathological inflammation in patients with COVID-19: A key role for monocytes and macrophages. *Nat. Rev. Immunol.* **20**, 355–362 (2020).
43. J. Liu, X. Han, T. Zhang, K. Tian, Z. Li, F. Luo, Reactive oxygen species (ROS) scavenging biomaterials for anti-inflammatory diseases: From mechanism to therapy. *J. Hematol. Oncol.* **16**, 116 (2023).
44. W. Royster, P. Wang, M. Aziz, The role of Siglec-G on immune cells in sepsis. *Front. Immunol.* **12**, 621627 (2021).
45. H. Shaim, H. Rafei, M. Kaplan, R. Basar, M. D. M. Daher, M. Shanley, P. Banerjee, B. Kumar, A. K. Nunez Cortes, S. Islam, X. R. Jiang, L. N. Kerbauy, P. Lin, E. Gokdemir, N. Uprety, S. Acharya, M. C. Mendt, L. Melo Garcia, A. Biederstädt, B. Liu, E. Liu, S. Ang, J. A. Burger, W. G. Wierda, A. Ferrajoli, E. J. Shpall, K. Rezvani, NK cell dysfunction in CLL is mediated through SHP-1 signaling and is associated with poor prognosis. *Blood* **142**, 1895 (2023).
46. G.-Y. Chen, X. Chen, S. King, K. A. Cavassani, J. Cheng, X. Zheng, H. Cao, H. Yu, J. Qu, D. Fang, W. Wu, X.-F. Bai, J.-Q. Liu, S. A. Woodiga, C. Chen, L. Sun, C. M. Hogaboam, S. L. Kunkel, P. Zheng, Y. Liu, Amelioration of sepsis by inhibiting sialidase-mediated disruption of the CD24-Siglec G interaction. *Nat. Biotechnol.* **29**, 428–435 (2011).
47. C. Loira-Pastoriza, J. Todoroff, R. Vanbever, Delivery strategies for sustained drug release in the lungs. *Adv. Drug Deliv. Rev.* **75**, 81–91 (2014).
48. K. Huang, Y. Liu, H. Miao, Y. Li, Q. Fan, H. Zhang, C. Zuo, J. Zhu, Q. Zheng, C. Deng, Z. Sun, Z. Tong, Nebulized lipid nanoparticles based on degradable ionizable glycerolipid for potent pulmonary mRNA delivery. *ACS Nano* **19**, 1128–1139 (2025).
49. Q. Yu, Q. Zhang, Z. Wu, Y. Yang, Inhalable metal–organic frameworks: A promising delivery platform for pulmonary diseases treatment. *ACS Nano* **19**, 3037–3053 (2025).
50. X. Murgia, B. Loretz, O. Hartwig, M. Hittinger, C.-M. Lehr, The role of mucus on drug transport and its potential to affect therapeutic outcomes. *Adv. Drug Deliv. Rev.* **124**, 82–97 (2018).
51. Q. F. Meng, W. Tai, M. Tian, X. Zhuang, Y. Pan, J. Lai, Y. Xu, Z. Xu, M. Li, G. Zhao, G. T. Yu, G. Yu, R. Chen, N. Jin, X. Li, G. Cheng, X. Chen, L. Rao, Inhalation delivery of dexamethasone with iSEND nanoparticles attenuates the COVID-19 cytokine storm in mice and nonhuman primates. *Sci. Adv.* **9**, eadg3277 (2023).
52. L. Yang, X. Xie, Z. Tu, J. Fu, D. Xu, Y. Zhou, The signal pathways and treatment of cytokine storm in COVID-19. *Signal Transduct. Target. Ther.* **6**, 255 (2021).
53. Y. Imai, K. Kuba, G. G. Neely, R. Yaghubian-Malhami, T. Perkmann, G. van Loo, M. Ermolaeva, R. Veldhuizen, Y. H. Leung, H. Wang, H. Liu, Y. Sun, M. Pasparakis, M. Kopf, C. Mech, S. Bavari, J. S. Peiris, A. S. Slutsky, S. Akira, M. Hultqvist, R. Holmdahl, J. Nicholls, C. Jiang, C. J. Binder, J. M. Penninger, Identification of oxidative stress and Toll-like receptor 4 signaling as a key pathway of acute lung injury. *Cell* **133**, 235–249 (2008).
54. Y. Ma, W. Sun, Z. Ye, L. Liu, M. Li, J. Shang, X. Xu, H. Cao, L. Xu, Y. Liu, X. Kong, G. Song, X. B. Zhang, Oxidative stress biomarker triggered multiplexed tool for auxiliary diagnosis of atherosclerosis. *Sci. Adv.* **9**, eadh1037 (2023).
55. M. J. Davies, Myeloperoxidase: Mechanisms, reactions and inhibition as a therapeutic strategy in inflammatory diseases. *Pharmacol. Ther.* **218**, 107685 (2021).
56. G. Y. Liu, G. R. S. Budinger, J. E. Dematte, Advances in the management of idiopathic pulmonary fibrosis and progressive pulmonary fibrosis. *BMJ* **29**, e066354 (2022).
57. Y. Ma, S. Li, X. Lin, Y. Chen, A perspective of lipid nanoparticles for RNA delivery. *Exploration* **4**, 20230147 (2024).
58. S. Liu, Y. Wen, X. Shan, X. Ma, C. Yang, X. Cheng, Y. Zhao, J. Li, S. Mi, H. Huo, W. Li, Z. Jiang, Y. Li, J. Lin, L. Miao, X. Lu, Charge-assisted stabilization of lipid nanoparticles enables inhaled mRNA delivery for mucosal vaccination. *Nat. Commun.* **15**, 9471 (2024).
59. P. Kesharwani, V. Kumar, K. W. Goh, G. Gupta, A. Alsayari, S. Wahab, A. Sahebkar, PEGylated PLGA nanoparticles: Unlocking advanced strategies for cancer therapy. *Mol. Cancer* **24**, 205 (2025).
60. L. Geddes, E. Themistou, J. F. Burrows, F. J. Buchanan, L. Carson, Evaluation of the in vitro cytotoxicity and modulation of the inflammatory response by the bioresorbable polymers poly(D,L-lactide-*co*-glycolide) and poly(L-lactide-*co*-glycolide). *Acta Biomater.* **134**, 261–275 (2021).
61. Y. Mitsui, T. Suzuki, K. Kuniyoshi, J. Inamo, K. Yamaguchi, M. Komuro, J. Watanabe, M. Edamoto, S. Li, T. Kouno, S. Oba, T. Hosoya, K. Masuhiro, Y. Naito, S. Koyama, N. Sakaguchi, D. M. Standley, J. W. Shin, S. Akira, S. Yasuda, Y. Miyazaki, Y. Kochi, A. Kumanogoh, T. Okamoto, T. Satoh, Expression of the readthrough transcript CiDRE in alveolar macrophages boosts SARS-CoV-2 susceptibility and promotes COVID-19 severity. *Immunity* **56**, 1939–1954.e12 (2023).
62. J. Nie, L. Zhou, W. Tian, X. Liu, L. Yang, X. Yang, Y. Zhang, S. Wei, D. W. Wang, J. Wei, Deep insight into cytokine storm: From pathogenesis to treatment. *Signal Transduct. Target. Ther.* **10**, 112 (2025).
63. L. P. A. Neyton, M. A. Matthay, C. S. Dela Cruz, A. N. Rizzo, Beyond immunosuppression: Decoding systemic immune dysregulation in ICU-acquired pneumonia. *Eur. Respir. J.* **65**, 2500185 (2025).
64. F. V. S. Castanheira, P. Kubes, Neutrophils and NETs in modulating acute and chronic inflammation. *Blood* **133**, 2178–2185 (2019).
65. A. J. Monteith, J. M. Miller, C. N. Maxwell, W. J. Chazin, E. P. Skaar, Neutrophil extracellular traps enhance macrophage killing of bacterial pathogens. *Sci. Adv.* **7**, eabj2101 (2021).
66. R. Zhang, C. Sun, Y. Han, L. Huang, H. Sheng, J. Wang, Y. Zhang, J. Lai, J. Yuan, X. Chen, C. Jiang, F. Wu, J. Wang, X. Fan, J. Wang, Neutrophil autophagy and NETosis in COVID-19: Perspectives. *Autophagy* **19**, 758–767 (2023).
67. X. Wang, M. Liu, J. Zhang, N. K. Brown, P. Zhang, Y. Zhang, H. Liu, X. Du, W. Wu, M. Devenport, W. Tao, Y. Mao-Draayer, G. Y. Chen, Y. E. Chen, P. Zheng, Y. Liu, CD24-Siglec axis is an innate immune checkpoint against metaflammation and metabolic disorder. *Cell Metab.* **34**, 1088–1103.e6 (2022).
68. C. S. Delaveris, A. J. Wilk, N. M. Riley, J. C. Stark, S. S. Yang, A. J. Rogers, T. Ranganath, K. C. Nadeau, C. A. Blish, C. R. Bertozzi, Synthetic Siglec-9 agonists inhibit neutrophil activation associated with COVID-19. *ACS Cent. Sci.* **7**, 650–657 (2021).
69. J. Chen, Y. Zou, C. Deng, F. Meng, J. Zhang, Z. Zhong, Multifunctional click hyaluronic acid nanogels for targeted protein delivery and effective cancer treatment in vivo. *Chem. Mater.* **28**, 8792–8799 (2016).
70. Y. Guo, Y. Ma, X. Chen, M. Li, X. Ma, G. Cheng, C. Xue, Y. Y. Zuo, B. Sun, Mucus penetration of surface-engineered nanoparticles in various pH microenvironments. *ACS Nano* **17**, 2813–2828 (2023).
71. P. Jagdale, A. Verma, D. K. Shah, Pulmonary pharmacokinetics of antibody and antibody fragments following systemic and local administration in mice. *Pharmaceutics* **16**, 1259 (2024).
72. A. M. Wollacott, M. F. Boni, K. J. Szretter, S. E. Sloan, M. Yousofshahi, K. Viswanathan, S. Bedard, C. A. Hay, P. F. Smith, Z. Shriver, J. M. Trevejo, Safety and upper respiratory pharmacokinetics of the hemagglutinin stalk-binding antibody VIS410 support treatment and prophylaxis based on population modeling of seasonal influenza A outbreaks. *EBioMedicine* **5**, 147–155 (2016).
73. X. Liu, B. Zhang, Y. Wang, H. S. Haymour, F. Zhang, L.-C. Xu, M. Srinivasarao, P. S. Low, A universal dual mechanism immunotherapy for the treatment of influenza virus infections. *Nat. Commun.* **11**, 5597 (2020).
74. J. Burch, M. Corbett, C. Stock, K. Nicholson, A. J. Elliot, S. Duffy, M. Westwood, S. Palmer, L. Stewart, Prescription of anti-influenza drugs for healthy adults: A systematic review and meta-analysis. *Lancet Infect. Dis.* **9**, 537–545 (2009).
75. S. Dohrmann, J. Levin, J. N. Cole, A. Borchardt, K. Amundson, A. Almaguer, E. Abelovski, R. Grewal, D. Zuill, N. Dedeic, G. Hough, J. Fortier, J. Donatelli, T. Lam, Z.-Y. Chen, W. Jiang, T. Haussener, A. Noncovich, J. M. Balkovec, D. C. Bensen, V. Ong, T. P. Brady, J. B. Locke, S. Flanagan, R. M. Hughes, J. L. Stein, L. W. Tari, Drug-Fc conjugate CD388 targets influenza virus neuraminidase and is broadly protective in mice. *Nat. Microbiol.* **10**, 912–926 (2025).
76. S. L. Waghorn, K. L. Goa, Zanamivir. *Drugs* **55**, 721–725 (1998).
77. Y. Wu, J. Park, Q. V. Le, J. Byun, J. Choi, E. Xu, J. Lee, Y. K. Oh, NET formation-mediated in situ protein delivery to the inflamed central nervous system. *Nat. Commun.* **15**, 10747 (2024).

Acknowledgments

Funding: This work was financially supported by the National Key R&D Program of China (2024YFA1210303 received by F.M.) and the National Natural Science Foundation of China (52373299 and 51973149 received by C.D.).

Author contributions: Conceptualization: C.D., Z.Z., and X.W. Methodology: C.D., Z.Z., M.Y., X.W., X.Z., F.Z., and S.W. Validation: X.W., X.Z., F.Z., and S.W. Formal analysis: X.W., M.Y., C.D., and Z.Z. Investigation: X.W., X.Z., F.Z., and S.W. Resources: C.D., M.Y., and Z.Z. Data curation: X.W., M.Y., C.D., and Z.Z. Visualization: X.W., X.Z., and F.Z. Supervision: C.D., M.Y., and Z.Z. Project administration: C.D., M.Y., and Z.Z. Writing—original draft: X.W., X.Z., and F.Z. Writing—review and editing: C.D., M.Y., F.M., and Z.Z. Funding acquisition: C.D. and F.M. **Competing interests:** The authors have filed a patent application (no. 202610989163.X, filed on 3 July 2026 by Soochow University) related to the technology described in this work. This is the only patent associated with this study, and the application is currently pending. C.D., X.W., X.Z., S.W., and Z.Z. are listed as inventors. The authors declare that they have no other competing interests. **Data, code, and materials availability:** All data and code needed to evaluate and reproduce the results in the paper are present in the paper and/or the Supplementary Materials. Details for obtaining the materials developed in this study are described in Materials and Methods.

Submitted 17 September 2025
Accepted 13 July 2026
Published 19 August 2026
10.1126/sciadv.aec3712

ScienceAdvances

ROS-responsive nanogels enable inhaled CD24 immunotherapy for selective hyperinflammation suppression in severe pneumonia

Xin Wang, Xiaofei Zhao, Fan Zhang, Siyu Wang, Fenghua Meng, Chao Deng, Mingzhou Ye, and Zhiyuan Zhong

Sci. Adv. **12** (34), eaec3712. DOI: 10.1126/sciadv.aec3712

Science Advances (ISSN 2375-2548) is published by the American Association for the Advancement of Science. 1200 New York Avenue NW, Washington, DC 20005. The title *Science Advances* is a registered trademark of AAAS.